AD-A110 007 ARMY MISSILE COMMAND REDSTONE ARSENAL AL GUIDANCE A--ETC F/G 14/2
PERFORMANCE OF LAMINAR RATE SENSORS.(U)
JUL 80 A R BARBIN, J C DUNAWAY
UNCLASSIFIED DRSMI/RG-80-29-TR NL

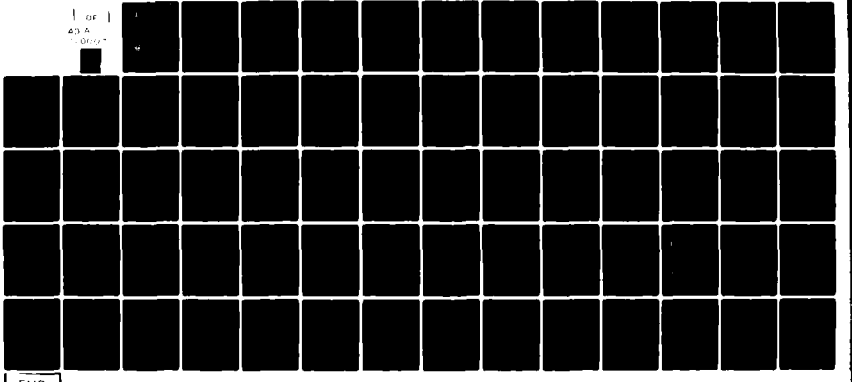

END
DATE FILMED
10-82
DTIC

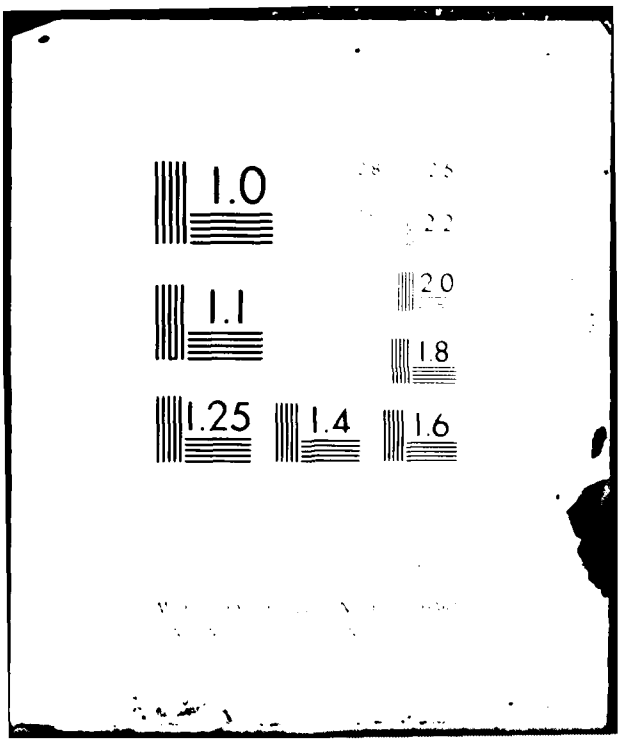
1.0
1.1
1.25
1.4
1.6
1.8
2.0
2.2

TECHNICAL REPORT RG-80-29

PERFORMANCE OF LAMINAR RATE SENSORS

A. R. Barbin and J. C. Dunaway
Guidance and Control Directorate
US Army Missile Laboratory

July 1980

U.S. ARMY MISSILE COMMAND
Redstone Arsenal, Alabama 35809

Approved for public release; distribution unlimited

DISPOSITION INSTRUCTIONS

DESTROY THIS REPORT WHEN IT IS NO LONGER NEEDED. DO NOT RETURN IT TO THE ORIGINATOR.

DISCLAIMER

THE FINDINGS IN THIS REPORT ARE NOT TO BE CONSTRUED AS AN OFFICIAL DEPARTMENT OF THE ARMY POSITION UNLESS SO DESIGNATED BY OTHER AUTHORIZED DOCUMENTS.

TRADE NAMES

USE OF TRADE NAMES OR MANUFACTURERS IN THIS REPORT DOES NOT CONSTITUTE AN OFFICIAL INDORSEMENT OR APPROVAL OF THE USE OF SUCH COMMERCIAL HARDWARE OR SOFTWARE.

UNCLASSIFIED

SECURITY CLASSIFICATION OF THIS PAGE *(When Data Entered)*

REPORT DOCUMENTATION PAGE		READ INSTRUCTIONS BEFORE COMPLETING FORM
1. REPORT NUMBER TR-RG-80-29	2. GOVT ACCESSION NO. AD-A110007	3. RECIPIENT'S CATALOG NUMBER
4. TITLE *(and Subtitle)* Performance of Laminar Rate Sensors		5. TYPE OF REPORT & PERIOD COVERED 6. PERFORMING ORG. REPORT NUMBER
7. AUTHOR(s) A. R. Barbin J. C. Dunaway		8. CONTRACT OR GRANT NUMBER(s)
9. PERFORMING ORGANIZATION NAME AND ADDRESS Commander, US Army Missile Command ATTN: DRSMI-RPT Redstone Arsenal, AL 35898		10. PROGRAM ELEMENT, PROJECT, TASK AREA & WORK UNIT NUMBERS
11. CONTROLLING OFFICE NAME AND ADDRESS Commander, US Army Missile Command ATTN: DRSMI-RPT Redstone Arsenal, AL 35898		12. REPORT DATE July, 1980 13. NUMBER OF PAGES 60
14. MONITORING AGENCY NAME & ADDRESS(*if different from Controlling Office*)		15. SECURITY CLASS. *(of this report)* Unclassified 15a. DECLASSIFICATION/DOWNGRADING SCHEDULE

16. DISTRIBUTION STATEMENT *(of this Report)*

Approved for public release; distribution unlimited.

17. DISTRIBUTION STATEMENT *(of the abstract entered in Block 20, if different from Report)*

18. SUPPLEMENTARY NOTES

19. KEY WORDS *(Continue on reverse side if necessary and identify by block number)*

Laminar Rate Sensor
Fluidics
Fluerics

20. ABSTRACT *(Continue on reverse side if necessary and identify by block number)*

Laminar rate sensors fabricated with present state-of-the-art etching techniques were studied and found to have undesirable features which include: (1) small signal output; (2) sensitivity of null to variation in supply pressure; and (3) sensitivity of gain to temperature.

Null sensitivity to supply pressure was considered to be most significant. Analysis showed that the following were contributors to null bias sensitivity: (1) asymmetry of flow separation from nozzle wall; (2) interference between the

DD FORM 1 JAN 73 1473 EDITION OF 1 NOV 65 IS OBSOLETE

UNCLASSIFIED

SECURITY CLASSIFICATION OF THIS PAGE *(When Data Entered)*

Item #20 con't)

jet control edge; (3) wall roughness; (4) plane-to-plane alignment; and (5) vent flow pattern asymmetries.

Schemes for adjusting the null bias to a zero slope region are presented. A temperature compensation technique is also presented which also interacted with the sensor null bias. These techniques will require individual tuning of each sensor.

CONTENTS

		Page
I.	INTRODUCTION	5
II.	PROBLEM AREAS	7
	A. Low Signal Levels	7
	B. Noise	7
	C. Null Shift	8
	D. Temperature Sensitivity	16
	E. Pressure Sensitivity	17
III.	NULL BIASING TECHNIQUES	18
IV.	SUMMARY AND CONCLUSIONS	23
	NOMENCLATURE	56
	REFERENCES	59

LIST OF TABLES

Table	Title	Page
I.	MDAC optimization tests	25
II.	Summary of laminar rate sensor performance	26
III.	Null variations of LRS for ± 2% supply pressure variation	27

LIST OF FIGURES

Figure	Title	Page
1.	Laminar rate sensor	28
2.	Laminar rate sensor planforms	29
3.	Geometry of interaction region of a laminar rate sensor	30
4.	Output of MICOM LRS, $\dot{\theta}$ = 1.15 deg/sec	31
5.	Null shift with supply pressure, σ = 1.25	32
6.	Null behavior as a function of stack configuration σ = 0.75	33
7.	Nozzle geometry	34
8.	Definition sketch - separation calculation	34
9.	Jet deflection at nozzle exit	35
10.	Saturation of LRS	36
11.	Gain curve of LRS	37
12.	Null output vs. supply pressure, σ = 1.25	38
13.	Jet deflection angles	39
14.	Velocity profile at Ps = 250 Pa	40
15.	Nozzle viewed from receiver port	41
16.	Null behavior, loose alignment pins, σ = 1.25	42
17.	Null behavior, tight alignment pins, σ = 1.25	43
18.	Null behavior, single laminate amplifier, σ = 3	44
19.	Effect of room air currents on noise and null drift	45
20.	Null drift - supply resistor upstream of solenoid	46
21.	Bench test setup - pressure regulation	47
22.	Repeatability of set point supply pressure	48
23.	Supply pressure long term drift and response to solenoid valve	49
24.	Effect of adjusting nozzle angle	50

LIST OF FIGURES (concluded)

Figure	Title	Page
25.	Biasing technique	51
26.	Control volume definition sketch	52
27.	Null behavior, constant bias resistances	53
28.	Null behavior, constant vent resistance	54
29.	Relation of zero slope and zero offset points	55

I. INTRODUCTION

A Laminar Rate Sensor (LRS) is a fluidic device which detects the deflection of a thin laminar jet relative to its rotating housing as a differential output across two receiver ports intercepting the jet. The fluid jet does not deflect relative to inertial space, rather, the receiver ports themselves move, due to rotation of the housing, out of a centered, zero-signal position relative to the jet. Figure 1 depicts the operation of the device. The apparent angle of deflection of the laminar jet, at a rotation rate of ω, is given by

$$\alpha = \omega t_f = \frac{\omega L}{V_{savg}} \qquad (1)$$

where t_f denotes the time of flight of a fluid particle from nozzle to receiver, V_{savg} the average nozzle (supply) velocity, and L is the splitter distance. Given that the output of the device is proportional to α, Equation (1) shows that this output is directly proportional to angular rate ω.

There has been a strong effort over the past decade to develop the laminar rate sensor to the stage where it could be integrated into a missile roll rate control system. This effort has not been a complete success. Problem areas have been identified, however, and some improvements in design and performance have been achieved. At present, some inherent limitations still exist on the use of the device.

Figure 2 illustrates several designs of rate sensor. Three early G. E. designs (Reference 1) are illustrated in Figures 2(i), 2(ii), and 2(iii). Each of these designs utilized a center dump vent and a 2-dimensional cavity in the free jet region. In addition, design 2(iii) had control ports and a cavity deeper than the supply nozzle. Designs I and II were plagued with problems caused by receiver tip vortices. Design III had a rather low momentum recovery which was attributed to the cavity depth. The splitter in designs 2(i), 2(ii), and 2(iii) was placed approximately 50 nozzle widths downstream. Tests on design 2(iii) utilizing two proportional amplifiers reportedly indicated a linear range of 400 deg/sec, a threshold of approximately 0.02 deg/sec, and a bias drift of 0.02 deg over 30 minutes. In light of later tests by McDonnell Douglass Astronautics Company (Reference 2) using a more accurate testing setup, no confidence can be placed in these numbers.

The rate sensor design illustrated in Figure 2(iv) was adapted by GE from a NASA/Langley design of a laminar proportional amplifier (Reference 3) which has a splitter distance of 9 nozzle widths. Originally, GE sought to improve the gain of a 3-stage laminar proportional amplifier (LPA) gain block. The stageable gain of the design 2(iv) was approximately 10. This LPA performed better than any of their designs as a laminar rate sensor (LRS) and it was adopted as the standard sensor in subsequent GE LARS work (Reference 4). It should be noted that GE had extreme difficulty staging their LPS's into a 3-stage gain block. Upon adding a third stage of amplification, noise levels increased dramatically, probably because all vents were tied together, allowing a feedback path to the vent and control ports of the LRS. As

recognized by GE, the laminate design was also a factor in the noise levels observed. Blocked port gains of the LRS, with no amplification, were reported to be

$$0.04 \frac{Pa}{deg/sec} \text{ at an aspect ratio of } \sigma = 0.6$$

and

$$0.067 \frac{Pa}{deg/sec} \text{ at } \sigma = 0.4$$

The use of stacked metal laminates to fabricate laminar rate sensors and laminar proportional amplifiers requires tighter tolerances than fluidic amplifiers operating in the turbulent flow regime. Entrainment rates of laminar jets are extremely small and, therefore, sensitive to the exiting velocity profile of the jet from the supply nozzle. Small asperities on the nozzle wall can affect these entrainment rates and the angle of the jet at the nozzle exit. GE found that identical planforms etched by Bendix from aluminum and titanium (dimensional repeatibility ~ 0.0025mm) showed remarkable improvement in null behavior and gain sensitivity ambient pressure changes over GE etched copper laminates (dimensional repeatibility ~ 0.025mm) (Reference 5). With this knowledge, GE ran a series of tests on devices which had been experimentally optimized in a rather clever way. Faulty laminates in a stack were identified by testing for null behavior before and after "flipping" of the laminate 180° about its longitudinal axis (Reference 6). In this way, grossly faulty laminates were eliminated. Tests of sensors so constructed (with amplification) were run with Bendix-fabricated stainless and titanium laminates. Null shifts from 0.067 to 0.40 deg/sec Pa supply pressure variation were encountered. It is of interest to note that there were measurable differences in those laminates held to the tightest dimensional control possible.

MDAC found that the rate sensors fabricated by GE exhibited excessive sensitivity to environments of altitude, temperature, vibration, and acoustics (Reference 7). Also, large null shifts with supply pressure were experienced. Threshold, resolution, and drift did not seem to be problem areas (at least for the 25-1000 °/sec systems tested). MDAC also tested Bendix titanium and stainless units. Noise in the stainless units were found to be significantly lower than either the copper or titanium units. A null shift of ~89°/sec over a supply pressure range of 1744 ± 124 Pa was measured.

A series of tests were performed by MDAC in an effort to optimize the geometry of the laminar rate sensor (Reference 7). Control port width, control edge width, splitter distance, receiver width, and aspect ratio were systematically varied to optimize gain. Figure 3 illustrates the geometry of the interaction region. Table I lists the range of parameters tested by MDAC and those chosen as "optimum".

The MDAC optimization tests were conducted at ambient temperature with vents sonically isolated from the surroundings (Pvent = 210 kPa). All of the planforms were etched by MDAC from 5-mil titanium, holding tolerances to 0.005mm.

A summary of the performance of various laminar rate sensors, as measured by MDAC, is presented in Table II. It is the opinion of this writer that little confidence can be placed in the tests conducted by GE*, and, thus, none are included in Table II. Also, the table does not include sensor amplifier packages. Thus, the performance figures listed pertain only to the sensor. Staged gain, noise, etc. could be quite different than the listed values, and would depend on the gain block design, etc. The numbers in Table II should be viewed as optimistic values since they represent the best performance numbers out of all tests run on the designated devices.

II. PROBLEM AREAS

At this stage of its development, the laminar rate sensor has several troublesome attributes. These are: (1) small signal levels; (2) noise; (3) null sensitivity to changes in supply pressure; and (4) degradation of performance with temperature change.

A. Small Signal Levels

As indicated in Table II, gains of laminar rate sensors are in the 0.08 - 0.30 Pa/(deg/sec) range with exact values depending on the planform design and the operating conditions. Amplification on the order of $\sim 5 \times 10^5$ is required to increase the signal to a useful level ($\sim$ 7 k Pa) for an angular rate of 1 deg/sec. Such amplification can be accomplished fluidically without introduction of extraneous noise if proper attention is paid to staging and manifolding techniques.

B. Noise

The noise levels given in Table II are, with the exception of the stainless unit, too large for use in a 1 deg/sec system. It is believed that the main sources of noise in a laminar rate sensor are the wall roughnesses caused by the etching process. The Bendix-etched titanium and stainless units had identical planforms with, ostensibly, identical dimensional repeatability ($\sim$0.003 mm); yet, the titanium unit had approximately 3 times the noise of the stainless unit. Figure 4 depicts the signal output of a stainless rate sensor fabricated at MICOM when operated at two different supply pressures. The noise levels observed are of the same order as that given in Table II for the Bendix unit. Also, the noise level (in equivalent deg/sec) is lower at the lower pressure. Roughly, the output varies directly as the supply pressure (i.e., as the square of the velocity) while the noise (as a percent of the output signal) varies as the square root of the supply pressure. (i.e., as the velocity).

---

*The reason for this lack of confidence is the accuracy of pressure measurement employed by GE($\sim$ 0.27 Pa) compared to that of MDAC ($\sim$ 0.0013 Pa). This necessitated (noisy) fluidic amplification of the signals with no way to infer blocked port gain of the sensor alone. GE did run some tests at NADC in 1975 (accuracy $\sim$ 0.013 Pa); however, the controls on the rate table burned out and the table had to be spun by hand with rate readings taken from a tachometer.

The size of the roughnesses on the nozzle walls is difficult to determine. No data can be found on the average roughness height for etched metal laminates. However, there does exist some information on etching of photoceramic materials. Fluidic devices etched from photosensitive glass consist of cavities with a floor. The depth of the cavity is determined by etching times. Van Tillburg (Reference 8) reports average roughness heights of ~0.0004mm on the cavity floors, but the walls were found to have roughnesses averaging ~0.0025mm. Since both were exposed to the same etchant, the relatively rough walls must be the result of the technique (artwork, exposure, etc.) used to transfer the planform pattern to the glass. The same technique is utilized to prepare metal laminates for etching and it is reasonable to suppose that metal laminates would have walls no smoother than the glass walls. Thus, in the absence of better information, we assume that the average roughness height on the nozzle is at least on the order of 0.0025mm.

C. Null Shift

Perhaps the most serious deficiency of a laminar rate sensor intended for use as a low angular rate sensing device is its null shift with supply pressure changes. Figure 5 illustrates this behavior. As indicated in the expanded curve (about the operating point), the slope of this curve is rather steep. The output signal corresponding to a rotation of 1 deg/sec is shown for comparison.

The exact shape of the null curve is a function of the fabrication and assembly of the device. To illustrate, Figure 6 shows the change in the null curve accompanying a change in position of the individual laminates in the stack (three 0.127mm stainless laminates). For identification, the laminates are numbered from the top cover plate in the first case (1-2-3), curve A in Figure 6. Also shown is the effect of rotating ("flipping") the center laminate about its longitudinal axis (contrast curves C and D). The implication of this behavior is that, with the present state of the art in fabricating etched metal laminates, the possibility of mass-producing sensors with predictable and repeatable null behavior is remote.

If it is supposed that the null shift is due entirely to misalignment of the downstream splitter, the angle of the jet with the centering of the device should not change and one would expect the null shift to be proportional to the dynamic pressure of the jet, i.e., to the supply pressure. However, this behavior is not observed. Evidently, the angle of the jet does change with supply pressure. Two causes could effect such a change. First, the separation points of the jet on either side of the nozzle could be slightly different due to slight radius differences and/or roughnesses just upstream of these points. Second, slight differences in nozzle wall roughness could affect the entrainment rates on either side of the jet and cause it to bend. In all likelihood, both effects are present to some extent. Each of these effects would be functions of the nozzle velocity.

Separation of the jet from the nozzle walls can be analyzed if the velocity profile at the nozzle exit can be estimated. Toward this end, consider the nozzle illustrated in Figure 7.

It is assumed that the boundary layer on the wall has zero thickness at the inlet to the converging section and, following Shearer and Smith

(Reference 9), the velocity profile within the boundary layer is taken to be sinusoidal. Thus

$$\frac{V}{V_p} = \sin\left(\frac{\pi Y}{2\delta}\right) \tag{2}$$

where Y denotes distance perpendicular to the wall, δ is the nominal boundary layer thickness, and V_p is the potential core velocity. For the converging section, from continuity

$$V_p = \frac{V_{sa}}{\frac{W}{B_s} - \frac{x}{B_s}\sin \alpha/2} \tag{3}$$

V_{sa} denotes the average velocity at the nozzle exit. For the nozzle under consideration (HDL design 3.1.1-005C)

$$W/B_s = 4.63$$

$$\alpha = 57^o$$

Equation (3) thus becomes

$$V_p = \frac{V_{sa}}{4.63-0.48\ x/B_s} \tag{4}$$

For the sinusoidal velocity profile, equation (2), it is not difficult to show that

$$\Theta = 0.1366\delta \text{ (momentum thickness)} \tag{5}$$

$$\delta^* = 0.3634\delta \text{ (displacement thickness)} \tag{6}$$

and

$$\tau = 1.5708\ \upsilon V_p/\delta \text{ (shear stress)} \tag{7}$$

The von karman momentum integral equation may be written as

$$\tau/\rho = V_p^2 \frac{d\Theta}{dx} + (2\Theta + \delta^*)V_p \frac{dV_p}{dx} \tag{8}$$

Using equations (4) - (7), equation (8) may be recast in the non-dimensional form

$$\frac{\delta^*/B_s}{4.63-0.48^{x}/B_s} \qquad \frac{d\left(\delta^*/B_s\right)}{d\left(x/B_s\right)} + \frac{2.237}{\left(4.63-0.48^{x}/B_s\right)^2}\left(\frac{\delta^*}{B_s}\right)^2 = \frac{1.519}{N_{Rb}} \tag{9}$$

where $N_{Rb} = V_{sa} B_s/\nu$, Reynolds number based on nozzle width some manipulation, equation (9) may be recast as

$$\frac{d}{dx}\left(N_{Rb}\phi\right) + \frac{4.474\left(N_{Rb}\phi\right)}{4.63-0.48x} = 14.066-1.458x \tag{10}$$

where $x = x/B_s$ and $\phi = \delta^{*2}$

Equation (10) is a first-order, linear, non-homogeneous differential equation which can be solved with the aid of an integrating factor. Its solution is

$$N_{Rb}\phi = (1-0.104x)^{9.29}\int \frac{14.066-1.458x}{(1-0.104x)^{9.29}}\,dx \tag{11}$$

A numerical integration of equation (11) from $x = 0$ to $x = 3.88$ yields a value of $(N_{Rb}\phi)$ at the inlet to the nozzle throat of

$$N_{Rb}\phi_i = 6.492$$

or

$$\sqrt{\phi_i} = \frac{\delta^*_i}{B_s} = \frac{2.548}{\sqrt{N_{Rb}}} \tag{12}$$

Equation (12) gives the displacement thickness at the entry to the throat of the nozzle. Schlichting's (Reference 10) solution for a parallel plat channel (entry region) should hold in the throat section. Thus,

$$\delta^*_t = k\sqrt{\nu(\ell ve + x_t)/V_{sa}} \qquad (k = 1.72) \tag{13}$$

where ℓve is equivalent length defined as that approach distance required to yield the displacement thickness given by equation (12) at $x_t = 0$. Thus

$$\frac{2.548}{\sqrt{N_{Rb}}} = k\sqrt{\frac{\nu\ell ve}{V_{sa}B_s^2}}$$

or

$$\mathrm{Re}_{/Bs} = \left(\frac{2.54}{k}\right)^2 = 2.195 \tag{14}$$

The displacement thickness at the exit of the nozzle is thus

$$\delta^*_E = k\sqrt{\frac{(2.195\ B_s + x_E)}{V_{sa}}}$$

or

$$\frac{\delta^*_E}{B_s} = k\sqrt{\frac{3.57}{N_{Rb}}} = \sqrt{\frac{3.25}{N_{Rb}}} \tag{15}$$

for the nozzle under consideration.

If it is assumed that the boundary layers on the side walls and end plates are equally thick, we can get an expression for the discharge coefficient of the nozzle. The volume rate Q can be expressed as

$$Q = V_{sa}\ B_s\ H \tag{16}$$

or, alternately, as

$$Q = V_{sp}\left(B_s - 2\ \delta^*_E\right)\left(H - 2\ \delta^*_E\right) \tag{17}$$

where V_{sp} denotes the potential core velocity at the nozzle exit and H is the height of the nozzle (i.e., the distance between the end planes). From (16 and (17),

$$V_{sp} = \frac{Vsa}{\left(1 - 2\frac{\delta^*_E}{B_s}\right)\left(1 - \frac{2}{\sigma}\frac{\delta^*_E}{B_s}\right)} \tag{18}$$

where $\sigma = {}^{H}/_{B_s}$. Expansion of equation (18), yields

$$\frac{V_{sp}}{V_{sa}} = \left(1 + 2\frac{\delta^*_E}{B_s} + \ldots\right)\left(1 + \frac{2}{\sigma}\frac{\delta^*_E}{B_s} + \ldots\right)$$

$$= 1 + 2\left(1 + \frac{1}{\sigma}\right)\frac{\delta^*_E}{B_s} + \ldots \tag{19}$$

If we neglect terms of order greater than (δ^*_E/B_s) we can get the approximate expression

$$V_{sp}/V_{sa} \quad 1 + \frac{2(1+\cdot)}{\cdot}\frac{\delta^*_E}{B_s} = 1 + \frac{6.50(1+\sigma)}{\sqrt{N_{Rb}}} \tag{20}$$

using equation (15). The discharge coefficient is simply the ratio of the average velocity at exit to the potential core velocity there. Thus,

$$C_D = \frac{V_{sa}}{V_{sp}} \quad \frac{1}{1 + \frac{\cdot+1}{\cdot}\frac{6.50}{\sqrt{N_{Rb}}}} \tag{21}$$

The point of separation of the flow from the nozzle side wall can be calculated (to within ~ 1°) with Stratford's technique (reference 11); (see Figure 8 for nomenclature). At the point of separation

$$C_p\left[(x - x')\frac{dC_p}{dx}\right]^2 = 0.0104 \tag{22}$$

where

$$C_p = 1 - V_p^2/V_{sp}^2 \quad \text{(pressure coefficient)} \tag{23}$$

$$x' = x_m - \int_0^{x_m}\left(\frac{V_p}{V_{sp}}\right)^5 dx = x_m - \frac{V_{sp}}{0.45\nu}\theta_E^2 \tag{24}$$

x designates the development distance (along the wall) of the boundary layer and x_m represents the minimum pressure point (point A in Figure 8); x_m is $5.179\ B_s$ for nozzle x' is the length of a flat plate required to develop a blasius profile at point A with the same momentum thickness, θ_E, as the actual boundary layer. The integral in equation (24) was evaluated using Walz' approximation (Reference 10).

The pressure coefficient of the flow downstream of point A, up to separation, can be found from the potential solution over the rear of a cylinder. Thus,

$$V_p = V_{sp}\cos\cdot$$

and

$$C_p = 1 - \cos^2\cdot = \sin^2\cdot \tag{25}$$

thus,

$$dcp/d_x = 2 \sin \gamma \cos \gamma \frac{d\gamma}{d_x} = \frac{2}{R} \sin \gamma \cos \gamma \tag{26}$$

Stratford's equation (22) may now be written as

$$\sin^2\left(\frac{x - x_m}{R}\right)\left[\frac{x-x'}{R} \sin\left(\frac{x-x_m}{R}\right) \cos\left(\frac{x-x_m}{R}\right)\right]^2 = 0.0104 \tag{27}$$

The term $(x-x')/R$ in equation (27) is simplified as follows: From equations (5) and (6),

$$\delta_E = 0.376\, \delta_E^* \tag{28}$$

Thus, from (24),

$$x' = x_m - \frac{V_{sp}\, \delta_E^{*2}}{3.185\nu}$$

or

$$\frac{x-x'}{R} = \frac{x-x_m}{R} + \frac{V_{sp}\, \delta_E^{*2}}{3.185\nu R} \tag{29}$$

Equations (15) and (19) can be utilized to express equation (29) as

$$\frac{x-x'}{R} = \frac{x-x_m}{R} + 3.317 \frac{B_s}{R}\left[1 + \frac{6.50(1+\sigma)}{\sigma\sqrt{N_{Rb}}}\right] \tag{30}$$

Substitution of equation (30) into (27) yields (after a bit of manipulation)

$$\left\{\gamma_s + 3.317 \frac{B_s}{R}\left[1 + \frac{6.50(1+\sigma)}{\sigma\sqrt{N_{Rb}}}\right]\right\} \sin \gamma_s \sin 2\gamma_s - 0.10198 = 0 \tag{31}$$

where $\gamma_s \equiv \frac{x_s - x_m}{R}$, the angle of separation.

Equation (31) indicates that the separation point depends on the Reynolds number and thus on the supply pressure. If both walls were of exactly the same radius, the separation points would be identical and the jet would remain centered. Consider, however, the situation depicted in Figure 9, where there exists a difference in radii on either side, and a small error Δ in the position of the centers of these radii. In this case, the jet will

make an angle β with the centerline of (Reference 12)

$$\beta = \arctan\left\{\frac{\Delta + R_2 \sin\gamma_{s_2} - R_1 \sin\gamma_{s_1}}{B_s + R_1\left(1 - \cos\gamma_{s_1}\right) + R_2\left(1 - \cos\gamma_{s_2}\right)}\right\} \tag{32}$$

and this angle will depend on N_{Rb}.

The effect of the jet angle β will show up as an output or null shift. It is presumed that saturation of the LRS occurs when the jet is deflected to the point where its ℓ intercepts the center of one receiver port (see Figure 10). This "saturation angle" is given by

$$\psi = \arctan\left(\frac{\Gamma}{L_R}\right) \tag{33}$$

for the MICOM LRS (with σ = 1.25), ψ = 2.684 deg.. The output associated with deflection β will be

$$\Delta Po = K\, Ps\, \frac{\beta}{\psi} \tag{34}$$

where K is the "gain" of the device. Figure 11 shows an input-output curve for the LRS used herein. For this device

$$K \simeq 0.77$$

Figure 12 is a plot of null output vs. supply pressure for the LRS with the gain curve shown in Figure 11. The LRS was operated with both control ports vented to ambient. The sensor was fabricated from five, 0.127mm stainless laminates (σ = 1.25), planform 3.1.1-005 C-mod.A. Utilizing equation (34), the jet deflection angles were calculated at several points. These angles are plotted in Figure 13. Also shown is a plot of jet deflection angles calculated from equations (31) and (32) with an assumed radius of 0.127mm on one wall and 0.114mm on the other. As indicated in the Figure, the jet deflection angles calculated from separation considerations vary only slightly with supply pressure (the analysis does not hold for Ps < 150 Pa since it predicts boundary layer thicknesses > Bs/2 there). The jet deflection angle derived from the null output data, however, varies linearly with supply pressure, except near Ps = 0 and beyond Ps ≃ 200 Pa. Thus, although some "steering" of the jet could be ascribed to the separation process at the nozzle exit, this cannot account for the observed behavior.

The region downstream of the nozzle exit and up to the control edge is illustrated in Figure 14, which also contains a calculated velocity profile at Ps=249 Pa. At this point the boundary layer thickness is ~ 0.22mm, which is large compared to the nozzle half-width of 0.254mm. The control edge setback for this LRS is quite small, 0.032mm from the jet centerline. At the conditions illustrated, separation is predicted at an angle $\gamma_s \simeq$ 2.85 deg. If the edge of the jet were to be at this angle, the Figure indicates that it would intercept the control edge (point P). It should be noted that

Manion and Drzewiecki's analysis predicts a clearance between the control edge and the entrainment streamline of -0.005mm for these conditions. It is clear that significant interference effects could exist in this amplifier because of the small control edge setback. Before ascribing the entire null behavior to this interference, however, we should recall that the null behavior of the optimum MDAC device was essentially no different from the present unit, even though it had a relatively large setback which allows for angles of spread (~11.7°) approximately 5 times those of the present device (~2.4°). Calculations have been made for the MDAC unit operating at P_s = 1.87 k Pa, σ = 0.50, which indicate a jet spread angle of ~1.5 deg.

It is clear from the foregoing, that the null behavior (i.e., shift) with operating pressure changes cannot be explained by changes in separation on the nozzle walls, nor is it related to jet control edge interference effects. The null shifts observed translate into jet deflection angles ~0.2 deg, approximately 10% of the angle required to saturate the device but ~325 times the deflection encountered by the jet in a rotation of 1 deg/sec, i.e. ~0.00062 deg. (from equation (1)).

At a rotation rate of 1 deg/sec, the jet deflection of 0.00062 deg translates into a lateral movement of 0.0001mm at the receiver ports. This is a distance some 27 times smaller than the dimensional repeatibility possible in etching metal laminates. When viewed in this way, it is indeed surprising that the LRS works as well as it does. These small distances suggest another possible explanation of the cause of the null shifts. When viewed from the receiver port, the nozzle appears as indicated in Figure 15. The walls are not perfectly smooth. As the supply pressure increases, the velocity profile flattens, the boundary layers on the top and bottom end plates become thinner, and those "layers" of fluid close to the plates exert an increasing influence on the total dynamic pressure. The same behavior translates to the splitter-receiver region where the momentum intercepted by the receivers is increasingly influenced (as supply pressure increases) by the fluid adjacent to the plates. As these regions near the plates (nozzle and splitter) are "uncovered" they can cause slight shifts in the momentum intercepted by the receivers. If the roughness elements are on the order of 0.0003mm, it is conceivable that they could effect strong enough changes to be measured.

Even if the walls were perfectly smooth, the metal planes could be misaligned, as indicated in Figure 15 (ii), and the same effect would be observed. There will always be some misalignment due simply to the dimensional repeatibility of siting the alignment pin holes in the laminates. Figure 16 illustrates how the null shift curve may be changed by shifting the planes in a stack with loose fitting pins. Each successive curve was run after loosening the clamping screws, tapping the cover plates, and then retightening the screws. We have already seen in Figure 6, that shifting the relative position of laminates in the stack, and "flipping" them can drastically alter the null curve. Figure 17 illustrates the same effect for a stack of five laminates with tight fitting pins. Seven curves are shown in Figure 17; #1 is a reference configuration. Curve #2 is the null behavior of the stack upon "flipping", i.e., rotating, 180° about the longitudinal axis, of the entire stack. One would expect a curve identical to curve #1 with a polarity change; however, this does not occur. The only difference between curves 1 and 2, other than polarity, is the vent flow which is allowed

to pass through only one of the end plates. Curve 3 through 7 were succesively derived by rolling the stack down one plane each time; curves 2 and 7 are identical, as expected.

At this point, it might be conjectured that the null shift behavior could be considerably improved if a LRS could be constructed from a single laminate, and thereby eliminate the problem of plane-to-plane alignment. To check this out, a null curve was run on a corning 1x CD, 0.25mm proportional amplifier. This amplifier was not intended to be a laminar proportional amplifier, nor a rate sensor. However, by operating in the laminar regime, we were able to get a rate signal (albeit small) and a null curve, which is presented in Figure 18. Even here, a null drift with pressure is observed.

D. TEMPERATURE SENSITIVITY

As part of their evaluation program of fluidic laminar rate sensors for the Naval Air Systems Command, MDAC (Reference 2) ran tests on laminar rate sensors (supplied by GE) at -46C, ambient, 38C, and 74C. Gain and noise were the two parameters most affected by temperature variations. A loss of gain was experienced with elevated temperatures, while gain increases were encountered at low temperature. Noise levels increased with both extremes with the colder temperature producing the largest increase.

On the basis of their tests, MDAC found that gains could increase as much as 1.5 times from ambient down to -46C (though all their tests did not indicate this) and it could decrease by a factor of 3.5 from ambient to 74C. This behavior is expected since the dynamic pressure of the jet decreases with temperature.

The increase in noise associated with increasing and decreasing the temperature is difficult to explain. It is believed to be related to the technique of temperature conditioning. Conditioning air was circulated around the sensors during testing by a blower mounted in a remote temperature chamber. The sensors were shielded from direct wind currents but they were vented to ambient. In the presence of air flow, noise can easily feed through to the vents of the sensor and show up in the output. Figure 19 illustrates the effect of turning on a room-type air conditioner approximately 12 feet from a test setup. Two effects are noted: (1) a long term drift which is due to a cooling (temperature) effect, and, (2) an increase in noise due to turbulent air flow over the test area from the circulating blower of the A/C unit. The increase in noise observed by MDAC in their temperature tests is believed to be of the same source.

The long term drift illustrated in Figure 19 is a result of the change of resistance with temperature of the dropping resistor upstream of the sensor. With a change of temperature, this resistance changes, the supply pressure changes, and the null drifts (see paragraph 3 above). This proved to be somewhat troublesome in the course of one series of tests which were initiated by energizing a normally-closed solenoid in the supply line. With the dropping resistor downstream of the solenoid and being influenced by the heating effect of the solenoid, the supply pressure drifted at the rate of ~0.025 Pa/sec whereas, with the resistor upstream of the solenoid, this driftrate was ~0.013 Pa/sec. Using the slope of the null curve at the operating point,

the predicted drift with time agrees very well with the observed null drifts, (Figure 20).

Gain change with temperature occurs primarily because of a change in the dynamic pressure $\frac{1}{2}\rho v^2$, of the jet. As temperature increases, viscosity increases and causes (for the same pressure drop) a decrease in velocity. To maintain the dynamic pressure constant as temperature increases, the pressure could be increased. Hsueh (Reference 13) has shown that if the supply pressure is made to vary as $T^{\alpha+\frac{1}{2}}$, where α is the temperature exponent of viscosity ($0.71 > \alpha < 0.5$), the dynamic pressure of the jet will remain essentially constant with temperature. It was also shown that the required pressure variation could be implemented by placing an orifice upstream of the nozzle with an area $\leq$ one-tenth of the nozzle area. The only experiment performed to date to verify the theory was performed by Hsueh on a nozzle. The pressure on the nozzle does indeed increase with a temperature increase, though it approaches the theoretical value for area ratios of 1/100 or less. The effect on gain has not been experimentally verified.

The nozzles utilized in laminar rate sensors have areas ranging from $0.129mm^2$, (0.508mm, σ = [illegible]) to $0.323mm^2$ (0.508mm, σ = 1.25). Compensating orifices for these nozzles will range from 0.127 - 0.203mm diameter at 1/10 area ratios. This should afford partial temperature compensation. In practice, however, this technique could not be used because of the null shift problem. To illustrate for proper temperature compensation between ambient and 74C, the pressure at the nozzle would have to increase by

$$P74/Pamb = \left(\frac{273 + 74}{273 + 21}\right)^{1.21} \simeq 1.22 \qquad (\alpha = 0.5)$$

an increase of 22%. Pressure changes of this magnitude would be manifested as rather significant, and unacceptable, null shifts.

E. PRESSURE SENSITIVITY

In view of the sensitivity of null to supply pressure, it is important to maintain accurate regulation of the pressure at the nozzle of a laminar rate sensor. The setup used in the tests on the MICOM LRS is illustrated in Figure 21.

To get an idea of the pressure regulation achievable, a series of tests was run, some of the results of which are presented in Figure 22 which illustrates the supply pressure vs. time upon manual opening of valve A. Several pressure histories are illustrated. The initial pressure overshoot and decay are apparently caused by the capacitance of the lines preceeding the solenoid; one does not observe this behavior when cycling the solenoid valve with the regulators loaded (Figure 23). As indicated in Figure 22, the spread in the various curves is ~10 Pa. Undoubtely, some of the variation is due to normal room temperature fluctuations between tests, though it is hard to quantify the effect. Ignoring the temperature effect, we can conservatively estimate the set point repeatability of the pressure regulation scheme of Figure 21 as ~10 Pa at a nominal operating point of 249 Pa, i.e., as ± 2% of set point pressure. There is no reason to suppose that a special

purpose regulator with the smae repeatability cannot be developed. The curve shown in Figure 23 illustrates a long term drift in supply pressure (~0.0125 Pa/sec) which is believed to be a temperature effect on the supply resistor. Also shown is the rapid response of supply pressure to opening and closing the solenoid valve upstream of the LRS. As indicated above, the transient associated with pressurization of the lines upstream of the regulators (Figure 22) is not present.

Reference to Figure 5 illustrates the effect of the supply pressure set-point on the pressure regulation requirements. For the case illustrated in Figure 5, operation of the device at a supply pressure of 143 Pa (i.e., at the flat spot of the null shift curve) would require a pressure regulation of ± 5 Pa (± 3.5%) to maintain null uncertainty of 0.50 deg/sec. If the same device were operated at 162 Pa, however, pressure would have to be maintained to ± 0.33 Pa (± 0.2%) to ensure the same null uncertainty. In comparing the null sensitivities of different sensors, care must be taken that each is operated at comparable points on the null curve. MDAC (Reference 7) made the claim that their "optimum unit" achieved an improvement of 2 orders of magnitude in null shift over the Bendix-fabricated stainless unit. Closer inspection reveals, however, that MDAC was comparing its unit's operation at a flat spot with Bendix unit's operation at a point removed from a flat spot, and that, in fact, the improvement was indeed modest (see below and Table III).

Null sensitivity to supply pressure changes, as conventionally quoted, can be misleading. A more meaningful specification of null behavior is the unit's sensitivity to percentage regulation about the operating point. Table III lists the sensitivities of several sensors in deg/sec, equivalent signal, per ± 2% of set-point pressure (the 2% figure is believed to be presently achievable). As indicated in the table, the stainless units are capable of holding null to within 0.2/ sec (equivalent signal) if operated at a flat spot on the null shift curve provided the pressure is maintained within ± 2% of the set point. It does not appear possible to hold the null below ~2/sec variation if the units are not operated at a flat spot.

Table III does not include the null offsets and null behavior of some of the early GE units since their outputs were extremely noisy. In terms of equivalent rate signals, null offsets can be large but they are not considered to be a problem since they can be compensated by biasing in the amplification chain downstream of the sensor; also, some biasing can be accomplished in the sensor itself (see Section III below).

III. NULL BIASING TECHNIQUES

The null behavior of laminar rate sensors can be influenced to some extent by controlling the pressure in the control ports or by adjusting the nozzle angle (with respect to the ℄ of the unit). Several techniques have been used, including:

(1) Control ports open to ambient
(2) Each control port blocked
(3) Control ports connected
(4) Each control port vented through adjustable resistors
(5) Nozzle block cantilevered and adjustable

(6) Control ports biased from supply with adjustable resitors.
(7) Sensor cantilevered about splitter-receiver and adjustable with adjustable nozzle walls.

In their optimization studies, MDAC (Reference 7) ran null shift curves on each of 24 units tested with techniques (1), (2), and (3) above. In some units, there appears to be little difference between the three configurations, while in others, drastic changes in null behavior occur. No general conclusions can be drawn about the relative merits of the three on the basis of these tests. None of the three provides the opportunity of adjustment which is considered desireable in view of the normal unit-to-unit differences encountered.

GE utilized technique (4) to control bias. On the basis of their experience with this approach, it cannot be recommended as practical. The amount of flow entrained by the sides of the laminar jet in contact with the control port is extremely small and exerts a proportionally small aspirating effect. Apparently, the control port pressure is extremely sensitive to the resistance and it is hard to set the desired bias. There is another disadvantage to this approach; any noise delivered to the vent feeds through to the control ports and is amplified thereby. This is believed to be the cause of the noise problems experienced by GE in their attempts to amplify the output of their sensors. The GE AW-12 amplifiers used downstream of the sensor are notoriously noisy; their venting into the common manifold could have been the reason that GE noted increases in the noise/signal ratio with the addition of each stage of amplification.

A laminar rate sensor was constructed at MICOM which had an adjustable cantilevered nozzle section. By moving the nozzle transverse to the centerline of the sensor, the shape of the null curve was considerably influenced. It was found that the "flat spot" on the null curve could be moved, as indicated in the sketch of Figure 24, but that in other respects the null shift with pressure was essentially unchanged.

Garrett has developed a rate sensor package for MICOM which utilizes the principle of nozzle angle adjustment via cantilevering of the nozzle-control port-vent region about the splitter area which is accomplished with small set screws and is a bit easier than the caming arrangement used in nozzle-block adjustments. Also included in the Garrett design is an adjustment which deflects the nozzle wall.

All of the tests on the MICOM sensors in this report used individual biasing of the control ports with adjustable orifices fed from the supply pressure, as indicated in the sketch of Figure 25(i). Also, the vent was collected and exhausted to ambient through an adjustable orifice. It seemed advisable not to use linear resistors as biasing elements since their resistances change with temperature; a null shift with temperature would be undesirable. In general, null offset can be adjusted, at any supply pressure, to a desired value by individually adjusting the bias controls, or by changing the vent resistance.

The equivalent circuit of the biasing scheme used is indicated in Figure 25 (ii). It is easily shown that the pressure difference across the

control port is given by

$$\Delta P_c = P_s \left\{ \frac{R_{j1}}{R_{c1} + R_v\left(\frac{R_c}{R_{c2}}\right)} - \frac{R_{j2}}{R_{c2} + R_v\left(\frac{R_c}{R_{c1}}\right)} \right\} \tag{35}$$

where

$$R_c = R_{c1} + R_{c2} + R_{j1} + R_{j2} \tag{36}$$

and

R_{c1}, R_{c2} = resistances of control biasing orifices
R_{j1}, R_{j2} = jet-control edge resistances
R_v = vent resistance

Manion and Drzewiecki (Reference 12) have shown that the jet-control edge resistance is proportional to the supply nozzle resistance, which is roughly proportional to $\sqrt{P_s}$. The other resistances are orifice types and it can be shown that each is also proportional to $\sqrt{P_s}$. Thus,

$$R_{c1}, R_{c2}, R_{j1}, R_{j2}, R_v \sim \sqrt{P_s}$$

Thus, from (35)

$$\Delta P_c \sim P_s \tag{37}$$

The control port pressure difference ΔP_c exerts a transverse force on the jet exiting from the nozzle at an angle β. The effect is to reduce (or increase) this angle and thereby to reduce (or increase) the output. Consider the control volume indicated in Figure 26. The net force in the Y-direction is $\Delta P_c A$, where A is the control port area. Using the momentum equation,

$$\Sigma F_y = \dot{m}\left(V_{yout} - V_{yin}\right) \tag{38}$$

$$\text{Thus, } -\Delta P_c A = \dot{m}\left(V_{sa} \sin \beta_1 - V_{sa} \sin \beta\right) \tag{39}$$

where β_1 designates the angle of the jet leaving the control volume. Since $\dot{m} = \rho A_s V_{sa}$,

$$\sin \beta_1 = \sin \beta - \frac{\Delta P_c A}{\rho A V_{sa}^2}$$

or, for small angles,

$$\beta_1 \sim \beta - \frac{\Delta P_c A}{\rho A_s V_{sa}^2} \tag{40}$$

From equation (37),

$$\Delta Pc \sim Ps \sim V_{sa}^{2}$$

thus, equation (40) may be rewritten as,

$$\beta_1 \simeq \beta - k_1 \tag{41}$$

The output of the sensor will be proportional to β_1 and to the dynamic pressure of the jet.

$$\Delta Ps = k_2 C_R Ps (\beta - k_1) \tag{42}$$

Where C_R is a "recovery" coefficient of the jet. C_R is expected to increase with Reynolds no. (i.e., Ps) since the boundary layer thickness (at nozzle exit) decreases. Assuming

$$C_R \sim Ps^n$$

where $n(>0)$ is unknown. Thus

$$\Delta Po = k_3 Ps^{n+1} \left[f(Ps) - k_1 \right] \tag{43}$$

where β has been expressed as a function of Ps, f(Ps) (see Figure 13).

The rate of change of ΔPo with Ps is given as

$$\frac{\partial(\Delta Po)}{\partial Ps} = (n+1)k_3 Ps^n (f - k_1) + k_3 Ps^{n+1} \frac{df}{dps}$$

$$= \frac{(n+1)\Delta Po}{Ps} + k_3 Ps^{n+1} \frac{df}{dps} \tag{44}$$

From equation (44) it is noted that a flat spot ($\frac{\partial \Delta Po}{\partial Ps} = 0$) and a zero null offset ($\Delta P = 0$) can occur at the same point only when $d\beta/dPs = 0$. For the unit illustrated in Figure 13, this point occurs near 225 Pa; at lower pressures $df/d\beta \neq 0$ and equation (44) indicates that we should not expect both a flat spot and zero null offset at pressures below 225 Pa. Figure 27 and 28 illustrate the effect (for a different unit than that of Figure 13). The null curves in Figure 27 were generated by holding resistances Rc_1, Rc_2 constant while varying Rv while those of Figure 28 were generated by holding Rv constant while varying Rc_1 and Rc_2. The same set of curves result with either technique. The minimum of each curve moves toward Ps = 0 as the point of zero null offset is decreased, whereas the maximum points increase. As indicated, the device can be operated at a flat spot over a wide range of supply pressures, but there is only one supply pressure at which both null offset and slope are zero (275 Pa for the unit shown). For the planform

used in this study there exists significant interference effects between the jet and the control edge at this pressure (see Figure 14).

Figure 13 indicates that at Ps < 200 Pa, β is roughly proportional to Ps.

$$\beta \simeq k_4 \, Ps \quad (75 \text{ Pa} \leq Ps \leq 200 \text{ Pa})$$

Thus, we can write equation (43) as

$$\Delta Po = k_5 \, Ps^{n+2} - k_6 \, Ps^{n+1} \tag{45}$$

From equation (45)

$$\frac{\partial(\Delta Po)}{\partial Ps} = (n + 2)k_5 \, Ps^{n+1} - (n + 1)k_6 \, Ps^{n} \tag{46}$$

If Ps_2 denotes the zero null offset pressure,

$$k_5 \, Ps_2^{n+2} - k_6 \, Ps_2^{n+1} = 0$$

or

$$k_6 = k_5 \, Ps_2 \tag{47}$$

Designating the point of zero slope as Ps_1, equation (46) yields

$$(n + 2)k_5 \, Ps_1^{n+1} - (n + 1)k_6 \, Ps_1^{n} = 0 \tag{48}$$

Using equation (47), equation (48) may be manipulated to yield

$$\frac{Ps_2}{Ps_1} = \frac{n + 2}{n + 1} \tag{49}$$

Equation (49) indicates that the ratio of $\frac{Ps_2}{Ps_1}$ should be a fixed value (see Figure 29). Inspection of the null curves of Figures 27 and 28 show that this is, indeed, the case and

$$\frac{Ps_2}{Ps_1} \simeq 1.54 \tag{50}$$

for all curves having a zero null offset. From this it is inferred that

$$m = 0.818 \tag{51}$$

It should be noted here that the use of linear resistors to bais the sensor could result in an improvement in the sensitivity of null output to supply pressure. Thus, if the resistances R_{c1}, R_{c2}, R_v were independent of Ps, then, from equation (35)

$$\Delta P_c = k_6 (P_s)^{3/2} \tag{52}$$

and equation (43) would become

$$\Delta P_o = k_3 P_s^{n+1} \left[f(P_s) - k_7 \sqrt{P_s} \right] \tag{53}$$

At low pressures, $f = k_4 P_s$ and equation (53) indicates that ΔP_o would still be a function of Ps. The slope is (upon some manipulation)

$$\frac{d(\Delta P_o)}{dP_s} = \frac{(n+1)\Delta P_o}{P_s} + k_3 P_s^{n+1} \frac{df}{dP_s} - \frac{1}{2} k_7 \sqrt{P_s} \tag{54}$$

Equation (54) admits the possibility of coincident zero null and zero slope points. It should also be remembered that linear resistors would be temperature sensitive and would cause the null to be temperature dependent.

IV. SUMMARY AND CONSLUSIONS

Laminar rate sensors fabricated with present state-of-the-art techniques have several undesireable features including: (1) small signal output, (2) sensitivity of null to variations in supply pressure, and (3) sensitivity of gain to temperature. Enough evidence is now on hand to indicate that significant improvement in these areas will not result from further attempts to optimize via simple geometric changes in the planform. Nor is it likely that novel biasing techniques will be discovered to ameliorate the difficulties.

Presently achievable blocked-port gains of laminar rate sensors fall in the range of 0.08 - 0.30 Pa/(deg/sec); staged gains can be as low as 1/2 of blocked port gains. Fluid amplification (with all the attendant difficulties of staging, manifolding, etc.) on the order of 5×10^5 is required to increase the signal to a useful level.

Null sensitivity to supply pressure remains the most troublesome aspect of the laminar rate sensor. The effect cannot be attributed solely to separation from the nozzle walls nor to interference between the jet and the control edge. Contributing factors are: (1) wall roughness; (2) plane-to-plane alignment; and, (3) vent flow pattern asymmetries. Significant improvement in the null behavior is highly unlikely with the present method of fabrication from stacks of etched metal laminates.

The sensitivity of a laminar rate sensor decreases with temperature. Compensation for this effect by maintaining the jet dynamic pressure constant requires an increasing nozzle supply pressure. It appears that this can be accomplished (at least partially). The procedure, however, would result in significant nullshift (with the units presently available) and thus it

cannot be considered as a viable solution. At present, ther exists no temperature compensation scheme which does not also affect null.

The performance of a laminar rate sensor in a 1 deg/sec system is likely to be marginal for the following reasons:

(1) The transverse movement of the jet due to a 1 deg/sec rotation is on the order of ~ 0.075×10^{-3}mm. A surface finish with roughness elements less than this would be in the superfinish catagory. With the etched laminates used at present surface roughnesses of ~ 2.5×10^{-3}mm are likely.

(2) Noise levels of 0.3 - 0.6 deg/sec equivalent signal.

(3) Null sensitivity to pressure requires tight pressure regulation of supply pressure. For ± 2% regulation of supply pressure, null can vary ± 2.5 deg/sec unless care is taken to operate at a zero slope point. Null variations at these flat spots is ~ 0.2 deg/sec for ± 2% supply pressure regulation.

(4) If the units are operated at a supply pressure where null offset is not zero, null will be temperature sensitive.

It has been found that a simple biasing scheme using adjustable orifices can be used to operate a LRS at a zero slope point over a range of supply pressures. Adjustable orifices (rather than linear resistors) are recommended in order not to create a temperature-dependent biasing scheme. There does exist one supply pressure at which both null and its slope are zero (for the MICOM sensor) and, for reasons (3) and (4) above, biasing and supply pressure should be adjusted to insure operation at this point. With the present fabrication techniques, this is expected to require individual attention to each unit built.

The integration of a LRS into a system will require attention to isolation of the vent of the device from ambient (preferably via sonic orifices). In addition, care should be taken to isolate the LRS vent from other vents in the system (e. g. downstream amplifiers) to minimize noise in the LRS output.

Table 1. MDAC OPTIMIZATION TESTS (Reference 7)

ITEM	RANGE	OPTIMUM UNIT
Control port width	1-8 B_s	6 B_s
Control edge width	1.5 - 6 B_s	3.5 B_s
Splitter Distance	8-20 B_s	16 B_s
Receiver width	1-2 B_s	1.5 B_s
Aspect ratio	0.25-1.25	0.5

TABLE II. SUMMARY OF LAMINAR RATE SENSOR PERFORMANCE (TEST BY MDAC)

IDENTIFICATION	LAMINATE			GAIN (Pa/deg)/sec	NULL* SENSITIVITY (deg/sec)/Pa	NOISE (°/sec)	HYSTERESIS (°/sec)	INFORMATION SOURCE (REFERENCE No.)
	MATL.	THICKNESS (mm)	TOLERANCE held (mm)					
GE-1000°/sec	Cu	0.102	0.025	0.292	1.75	7	74	[2]
Bendix	S-S	0.051	0.003	0.096	0.15	0.6	0.43	[2]
Bendix	Ti	0.051	0.003	0.089	1.55	1.8	4.5	[2]
MDAC-Baseline	Ti	0.127	0.005	0.110	0.75	15	31	[7]
MDAC-Optimum	Ti	0.127	0.005	0.088	0.07	8	16	[7]

*Null Sensitivity is here defined as the slope of the null vs. supply pressure curve near the operating supply pressure.

TABLE III: NULL VARIATIONS OF LRS FOR ± 2% SUPPLY PRESSURE VARIATION.

UNIT	OPERATION AT FLAT SPOT		OPERATION OFF FLAT SPOT	
	Ps(kPa)	NULL VARIATION (deg/sec)	Ps(kPa)	NULL VARIATION (deg/sec)
MICOM (s-s)	0.143	0.16	0.162	±2.46
MDAC Optimum Unit(Ti)	1.87	2.76	1.96	±3.11
Bendix (s-s)	1.43	*0.13	1.50	±4.44
GE-200°/sec (cu)	1.42	0.81	1.37	±1.67
GE-1000°/sec (cu)	**	. . .	1.64	±57.4
Bendix-200°/sec (Ti)	1.21	*~10	1.50	±41

*These numbers are estimates of questionable accuracy because of the scale of the curves given in Reference (2).

**This unit had a hysteresis loop near its flat spot.

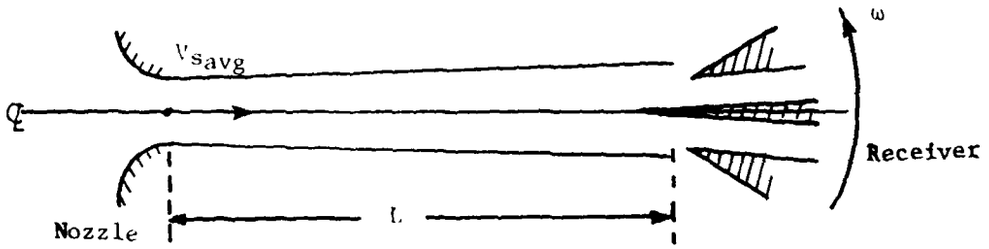

Figure 1. Laminar rate sensor.

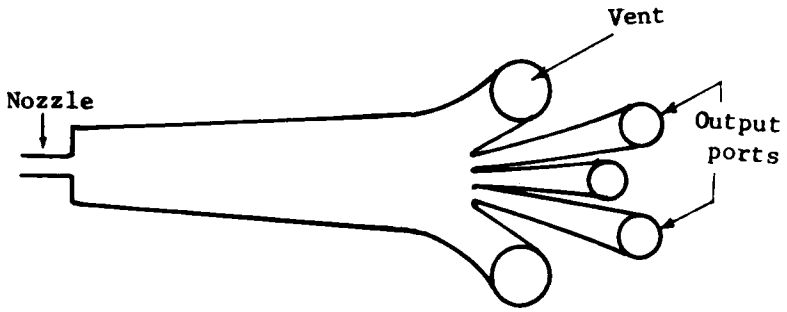

(i) GE type I

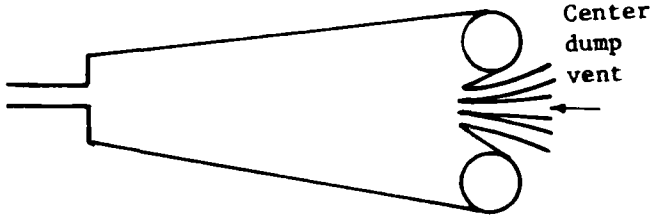

(ii) GE type II

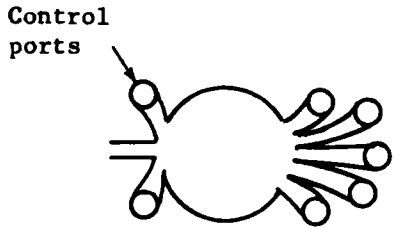

(iii) GE design with control vents

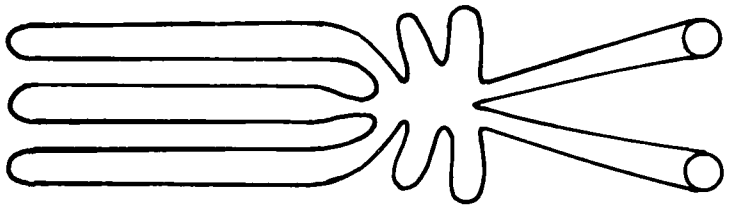

(iv) Modified NASA-HDL design

Figure 2. Laminar rate sensor planforms.

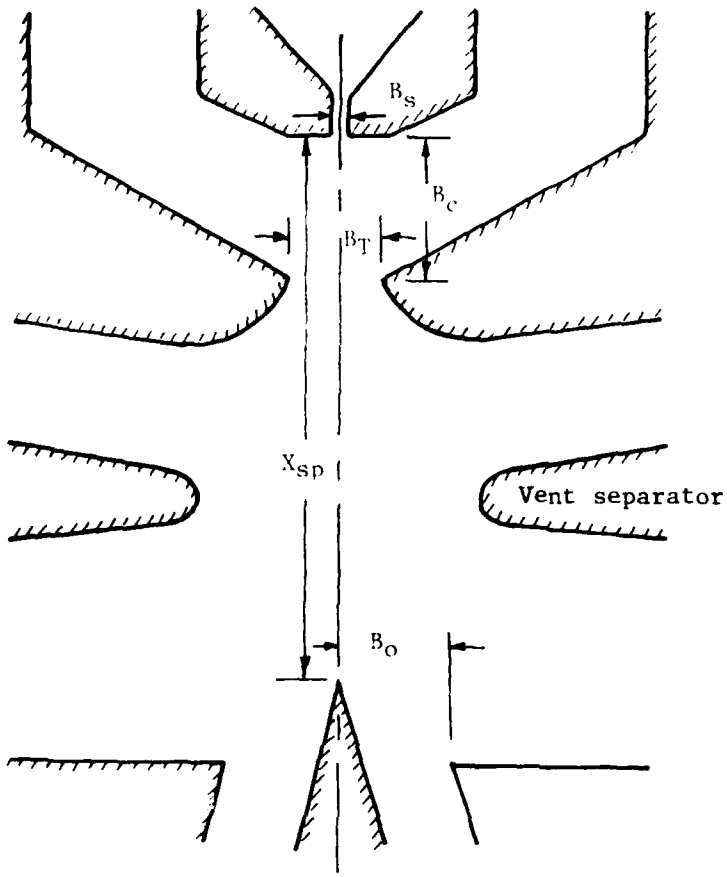

B_s = Nozzle width
B_c = Control port width
B_T = Control edge width
X_{sp} = Splitter distance
B_o = Receiver width

Figure 3. Geometry of interaction region of a laminar rate sensor.

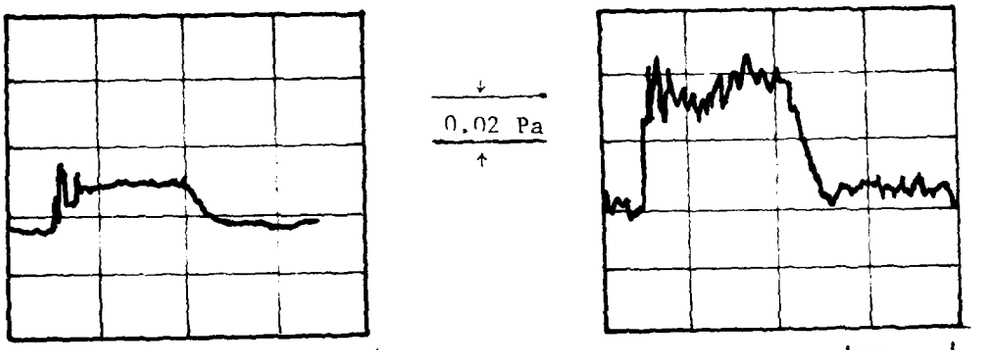

Figure 4. Output of MICOM LRS, ω = 1.15 deg/sec.

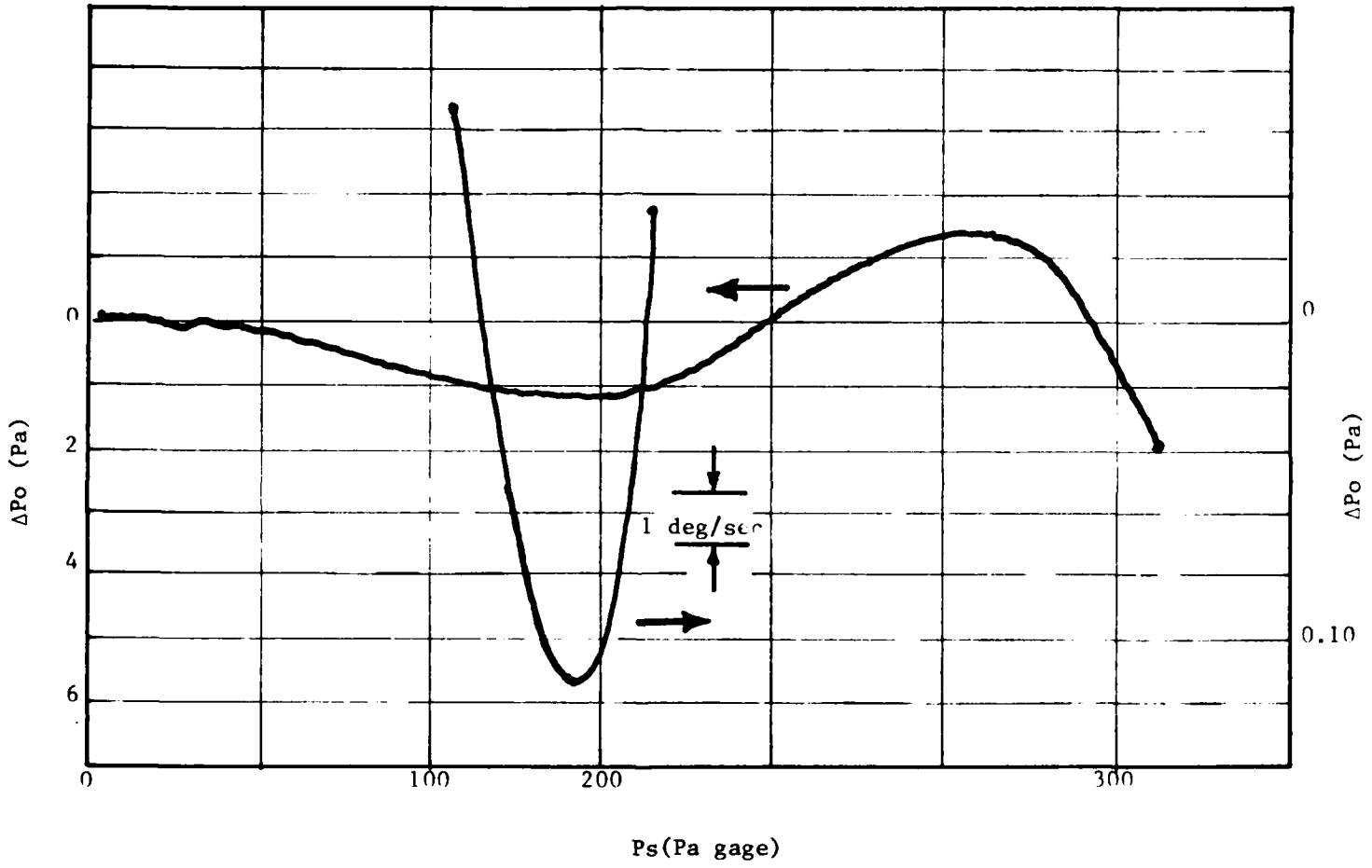

Figure 5. Null shift with supply pressure, σ = 1.25.

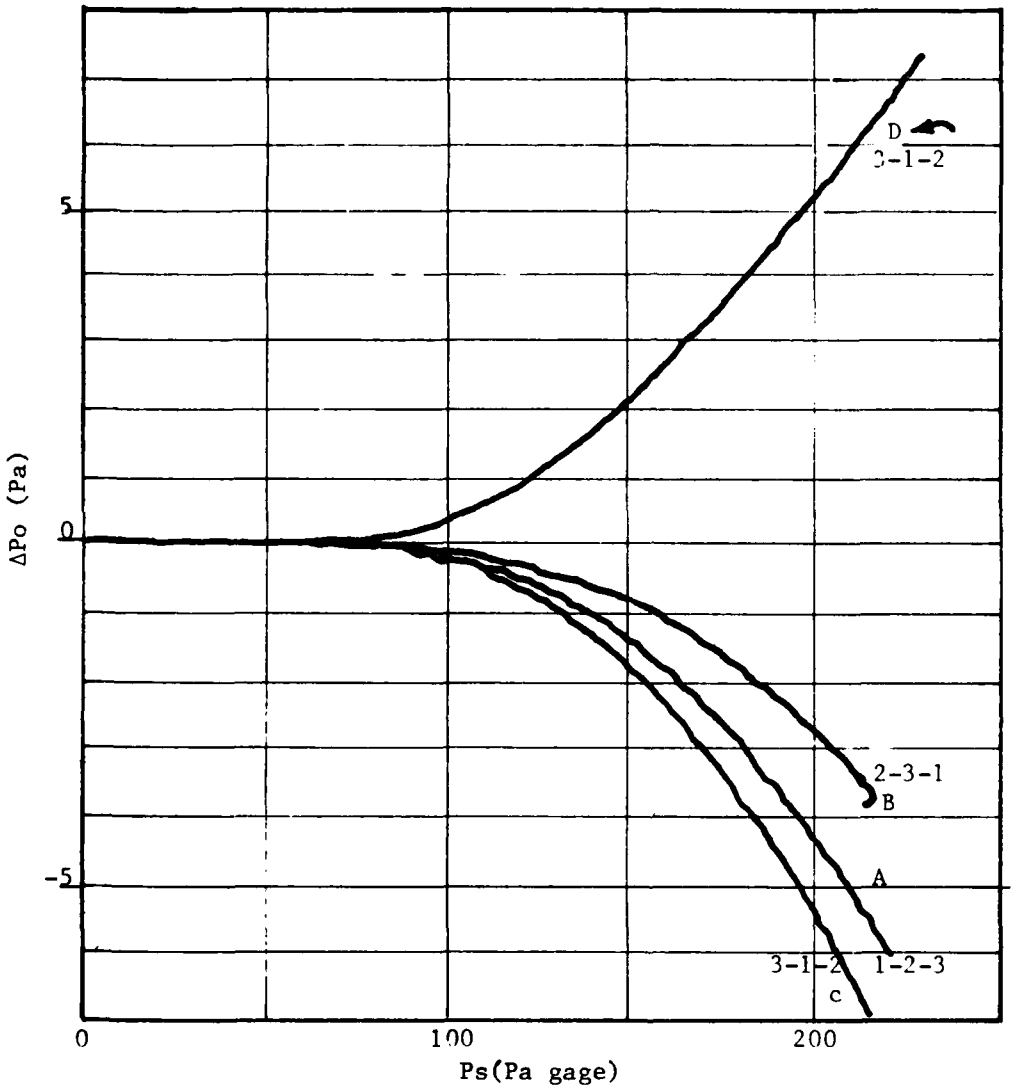

Figure 6. Null behavior as a function of stack configuration, σ = 0.75.

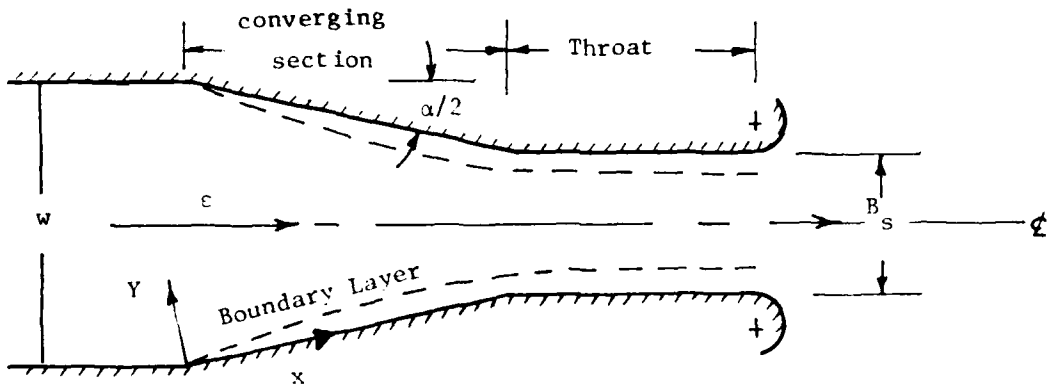

Figure 7. Nozzle geometry.

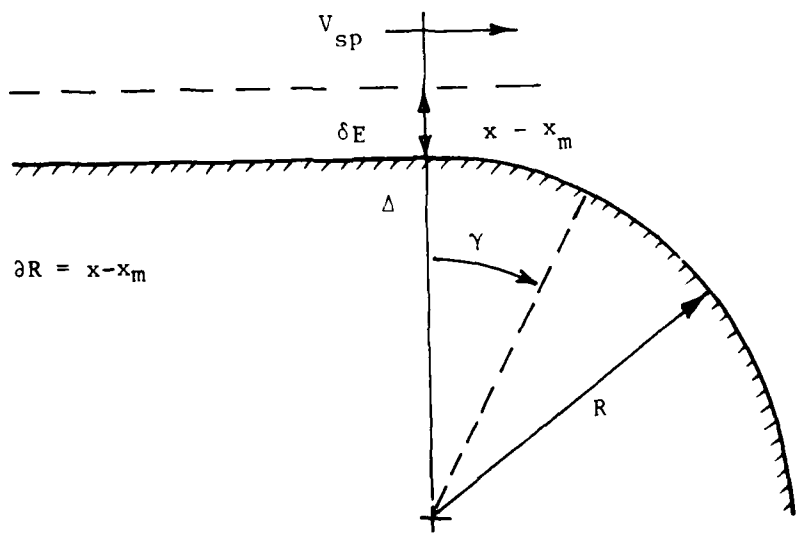

Figure 8. Definition sketch - separation calculation.

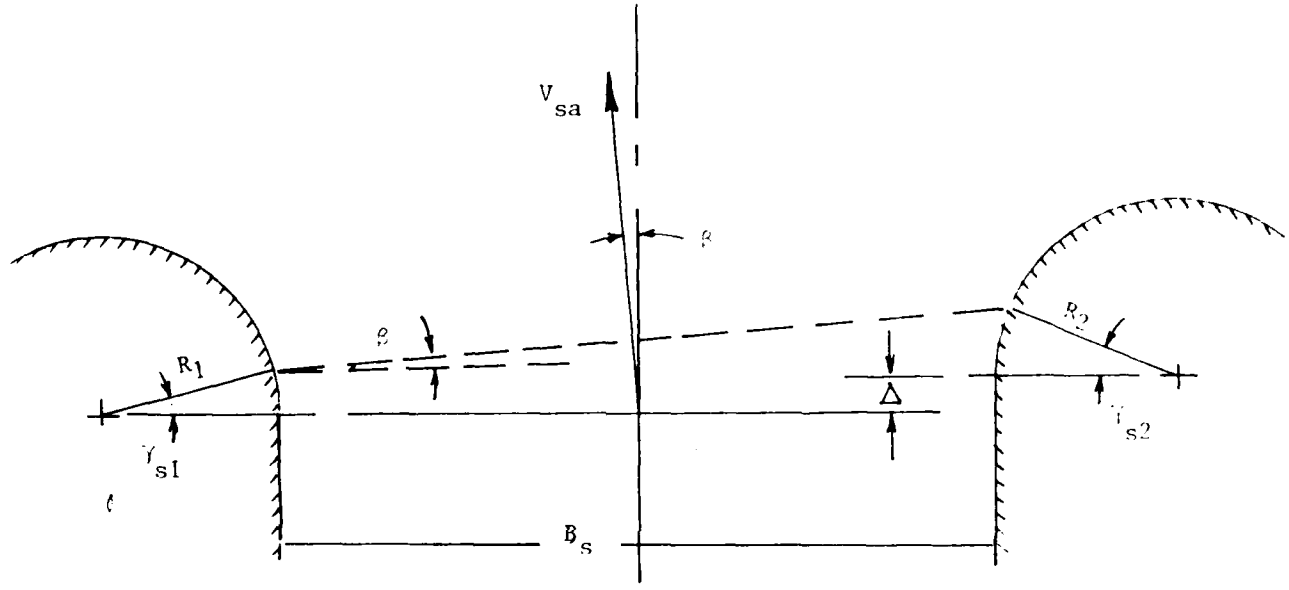

Figure 9. Jet deflection at nozzle exit.

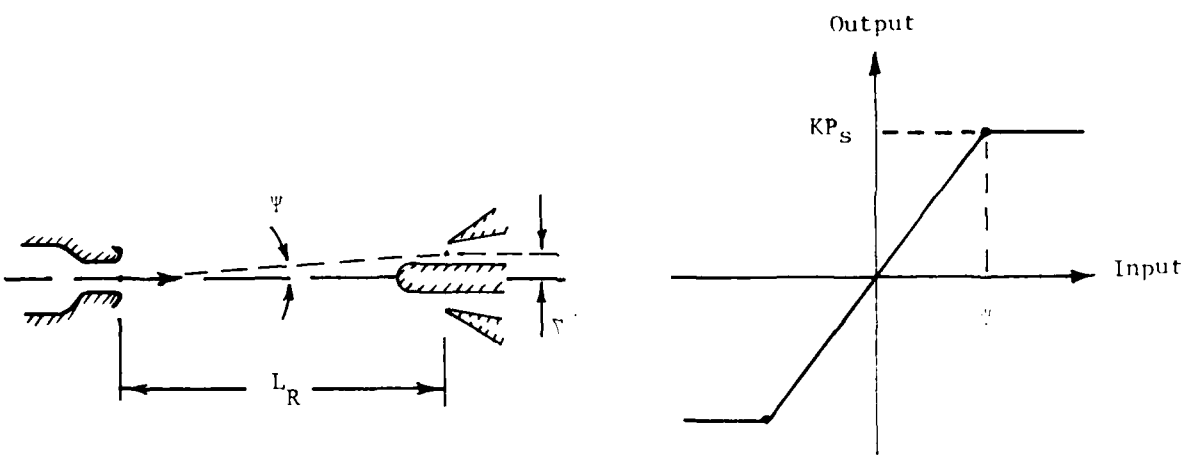

Figure 10. Saturation of LRS.

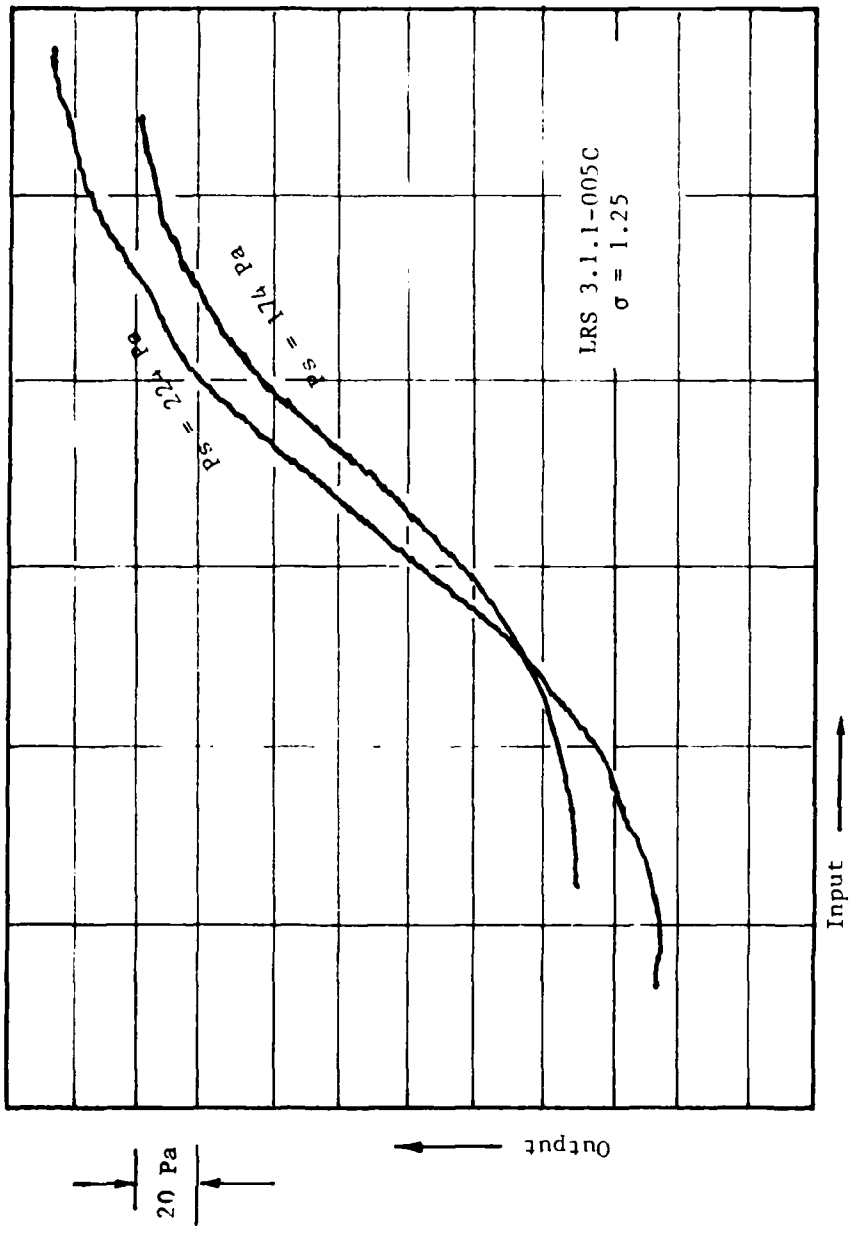

Figure 11. Gain curve of LRS.

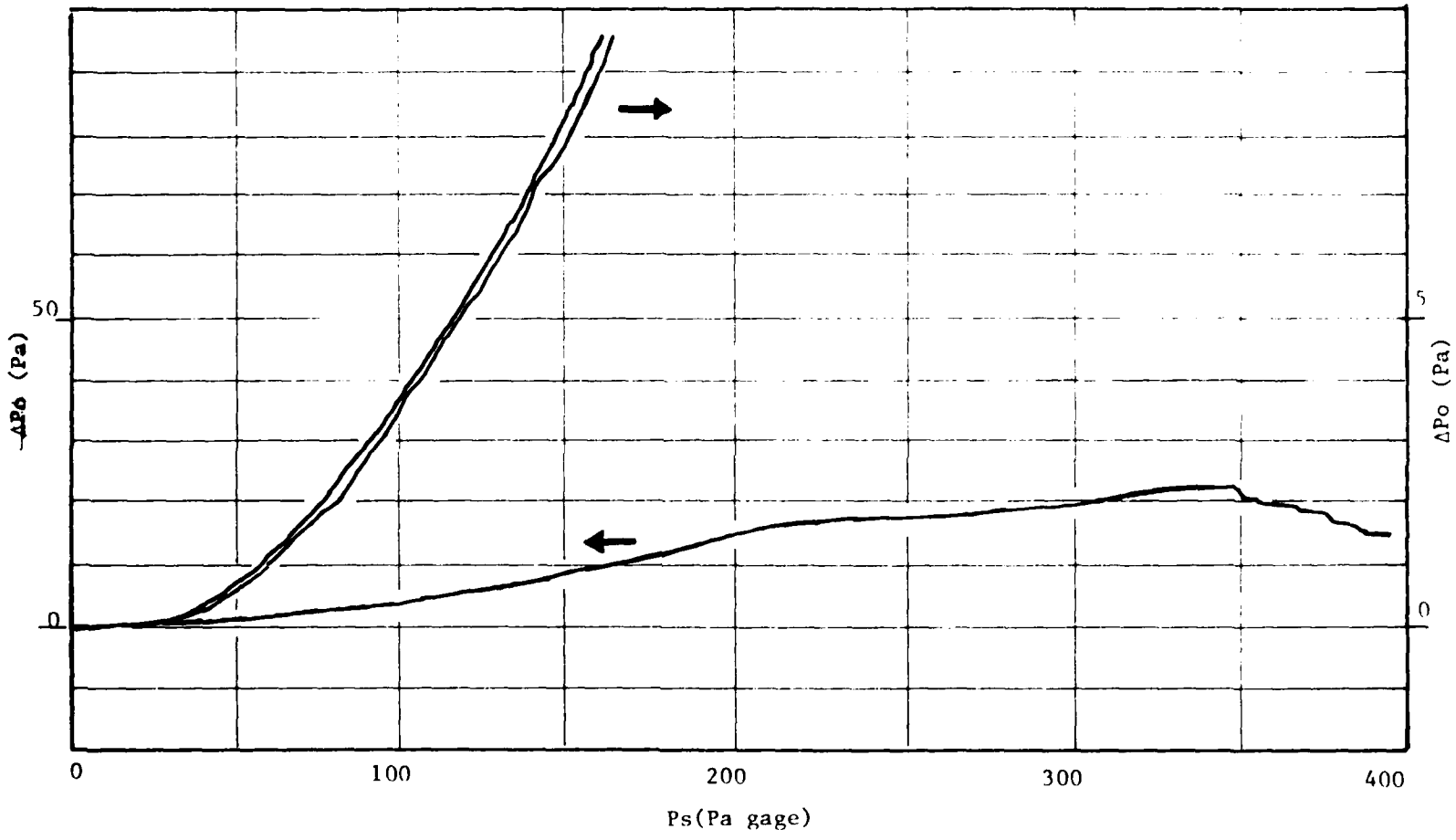

Figure 12. Null output vs. supply pressure, σ = 1.25.

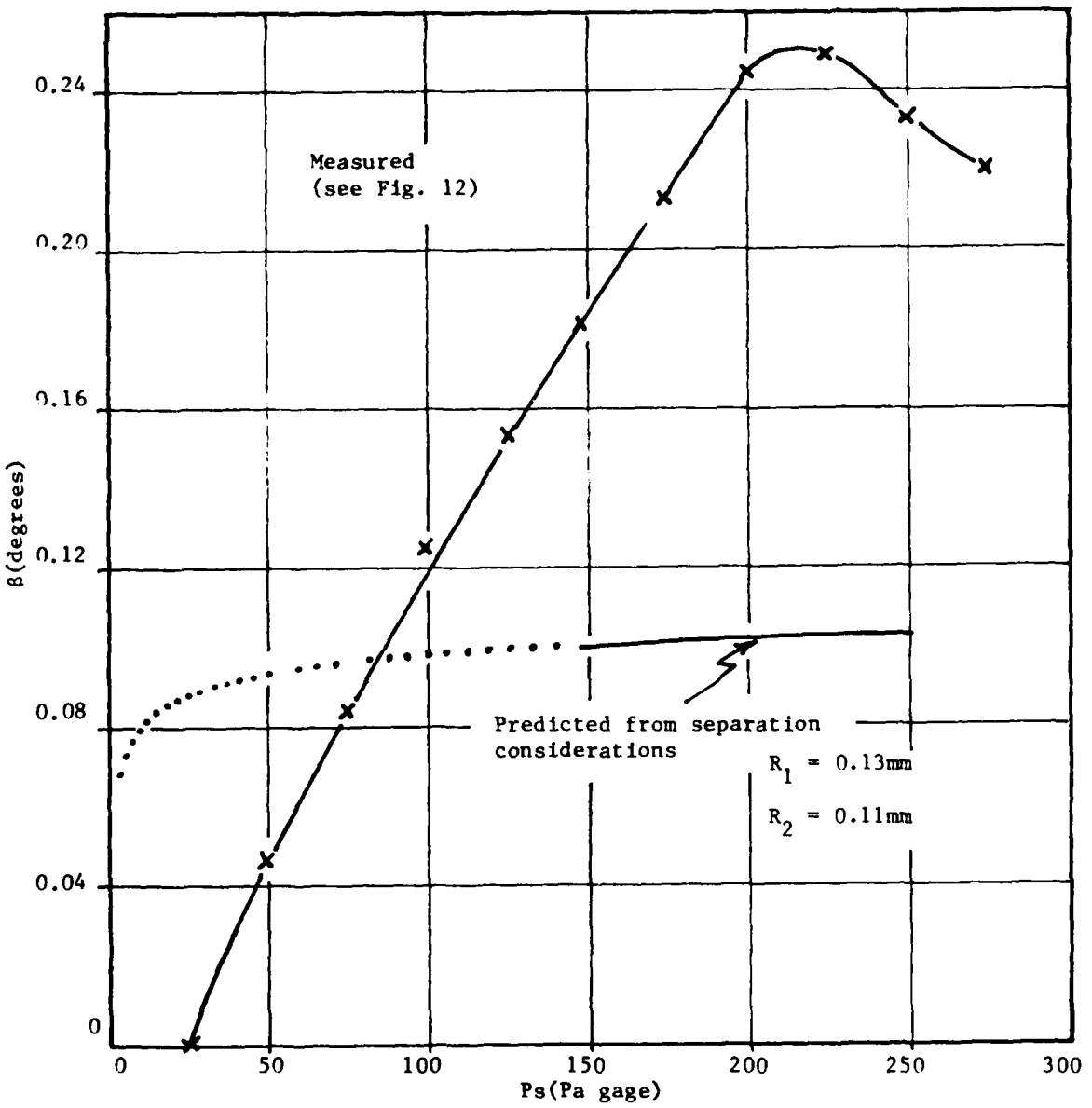

Figure 13. Jet deflection angles.

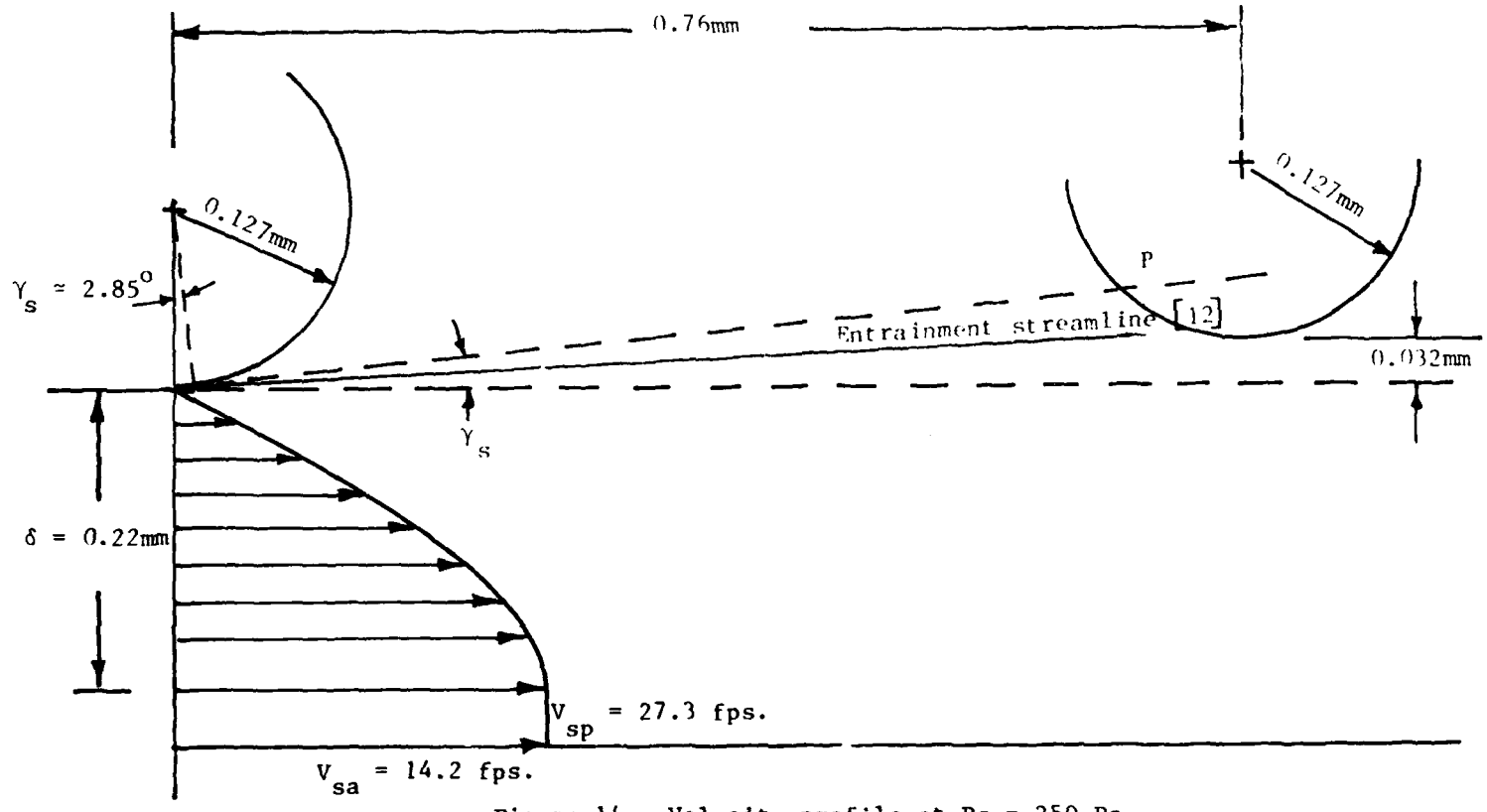

Figure 14. Velocity profile at Ps = 250 Pa.

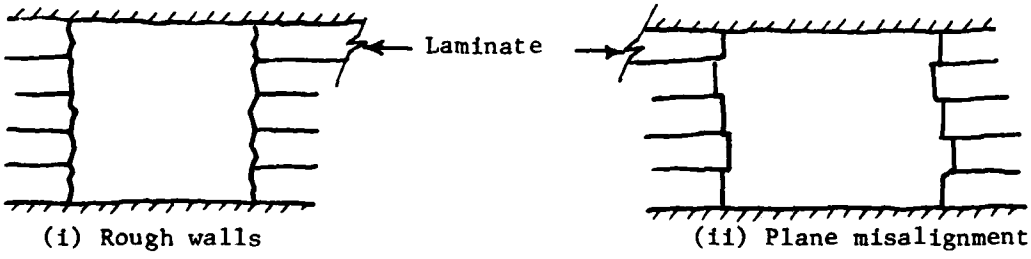

Figure 15. Nozzle viewed from receiver port.

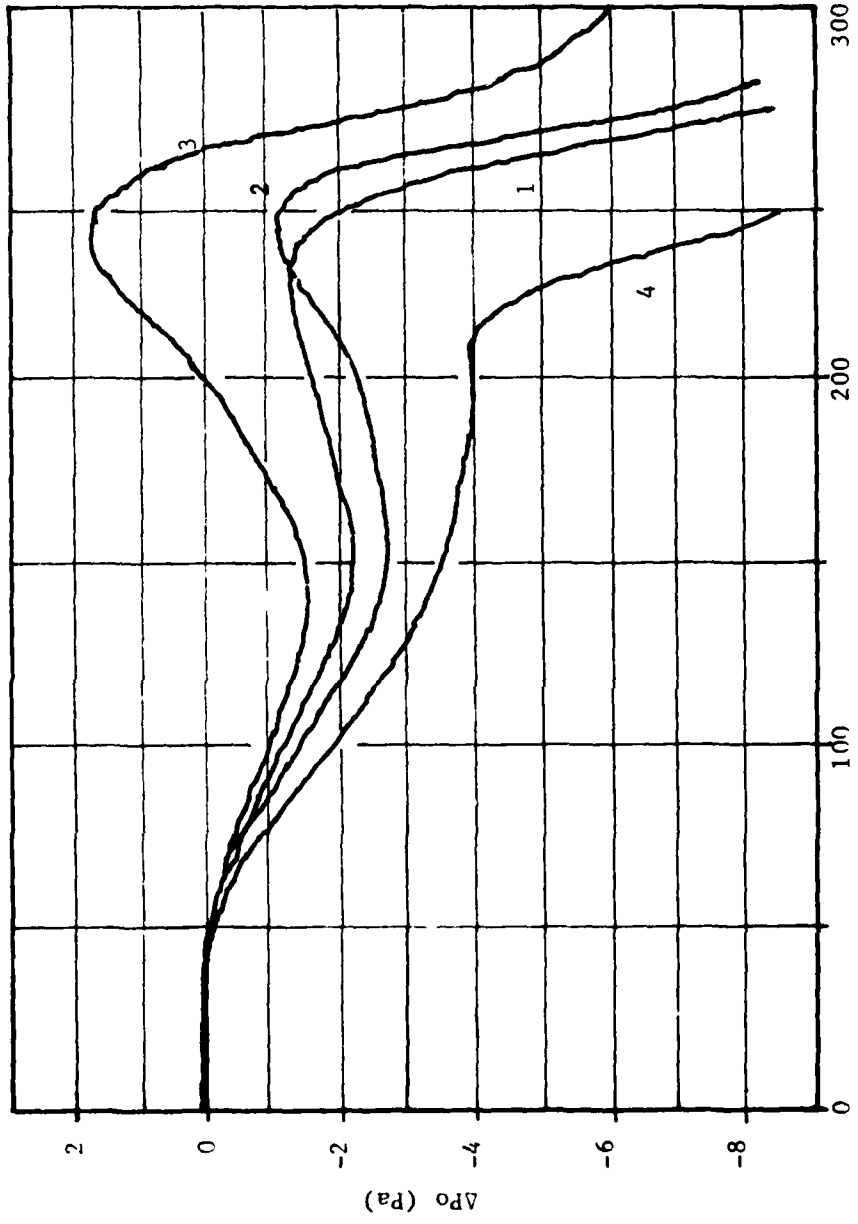

Figure 16. Null behavior, loose alignment pins, $\sigma = 1.25$.

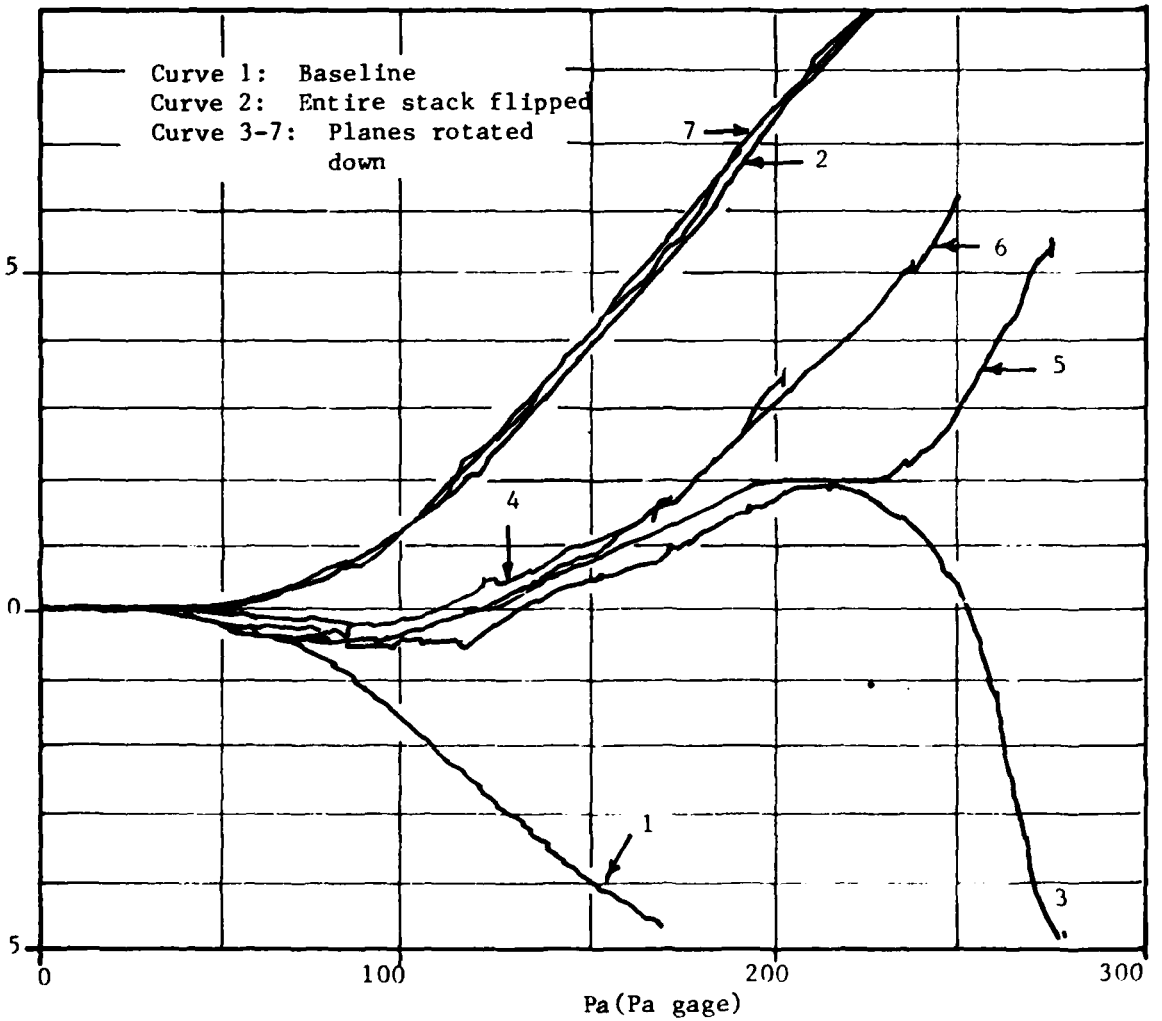

Figure 17. Null behavior, tight alignment pins, σ = 1.25.

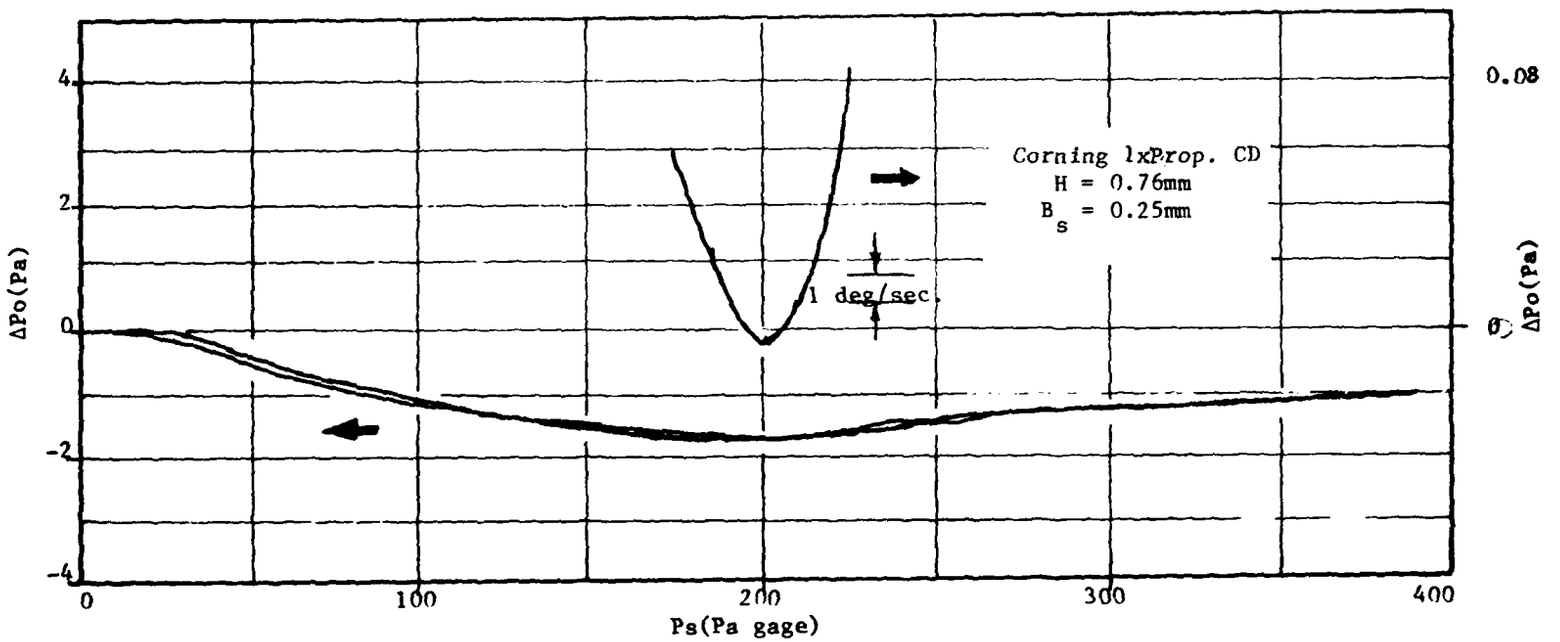

Figure 18. Null behavior, single laminate amplifier, σ = 3.

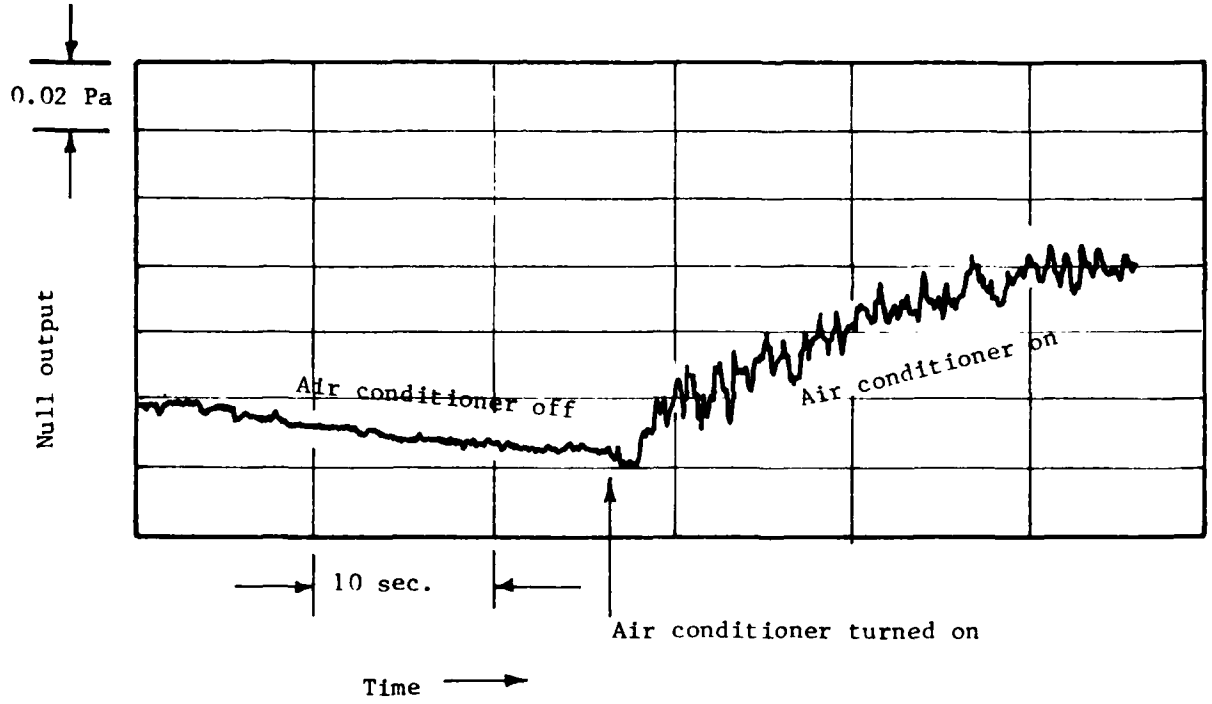

Figure 19. Effect of room air currents on noise and null drift.

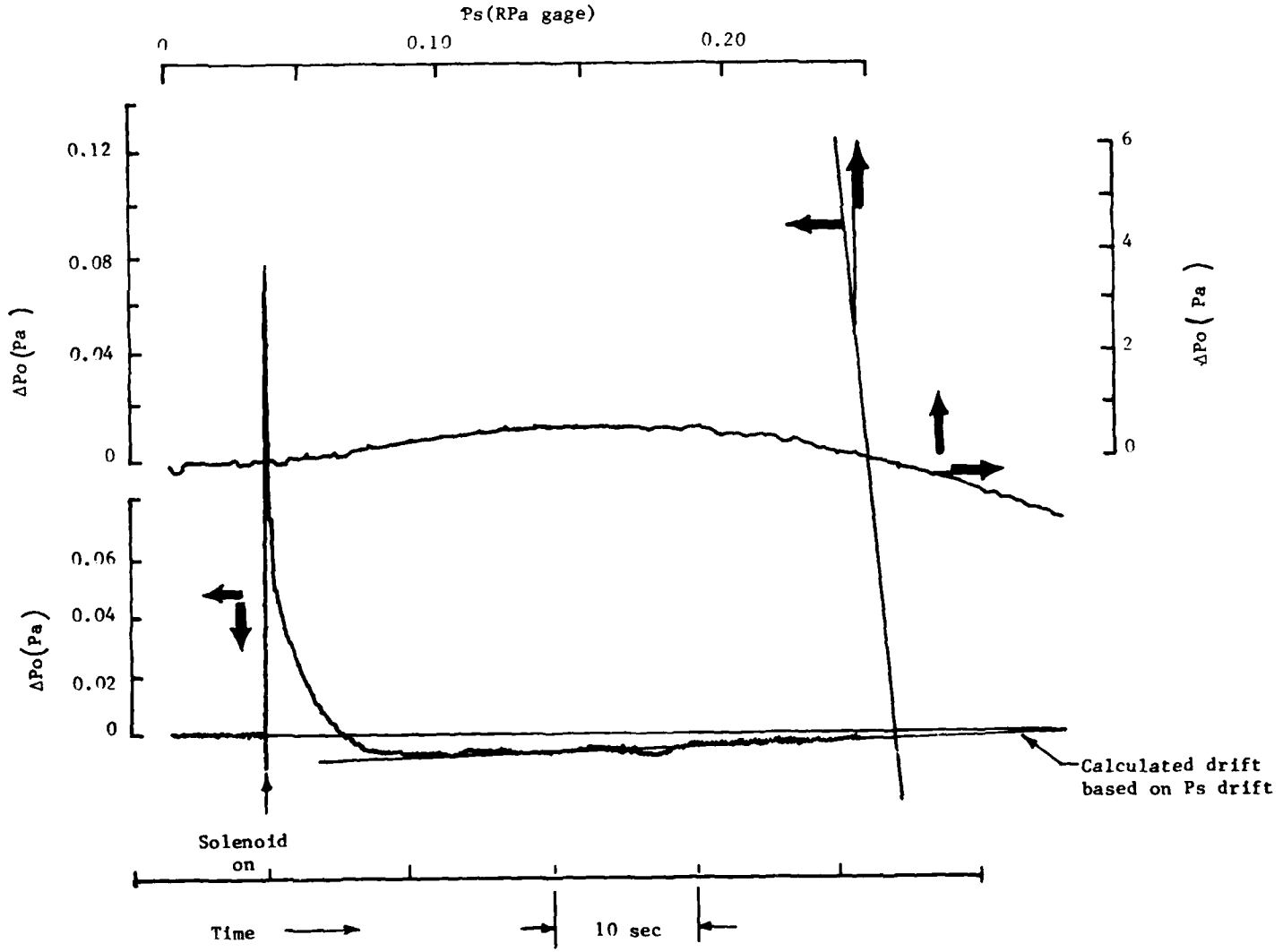

Figure 20. Null drift - supply resistor upstream of solenoid.

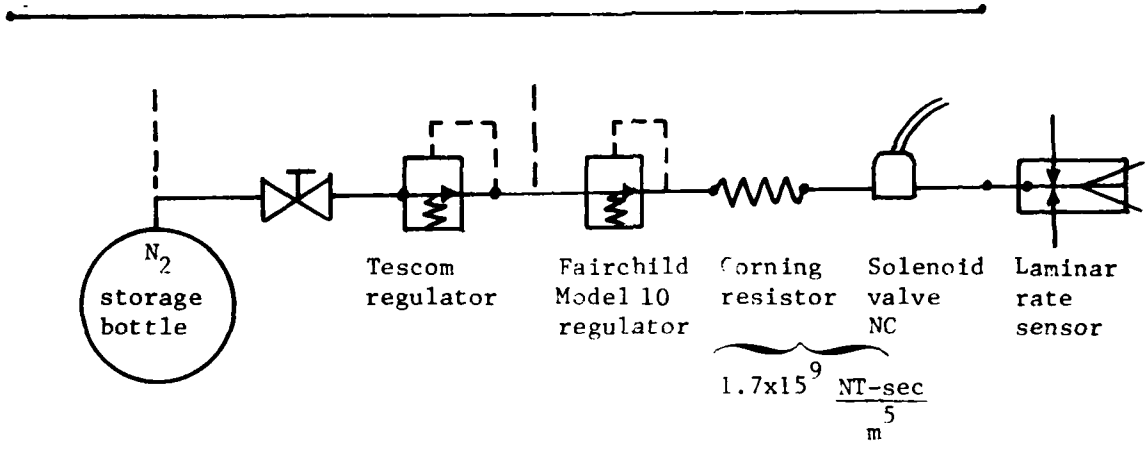

Figure 21. Bench test setup - pressure regulation.

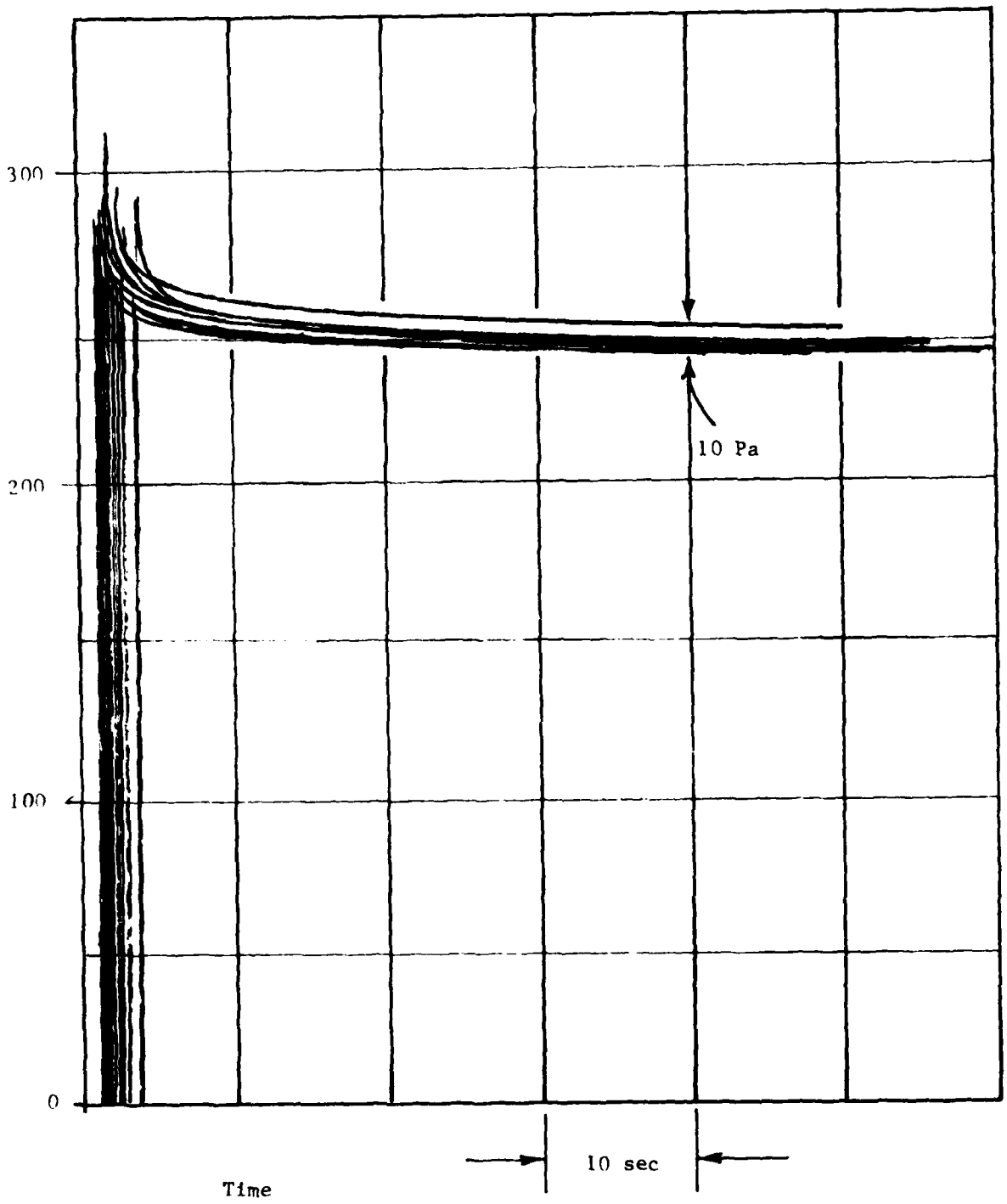

Figure 22. Repeatability of set point supply pressure.

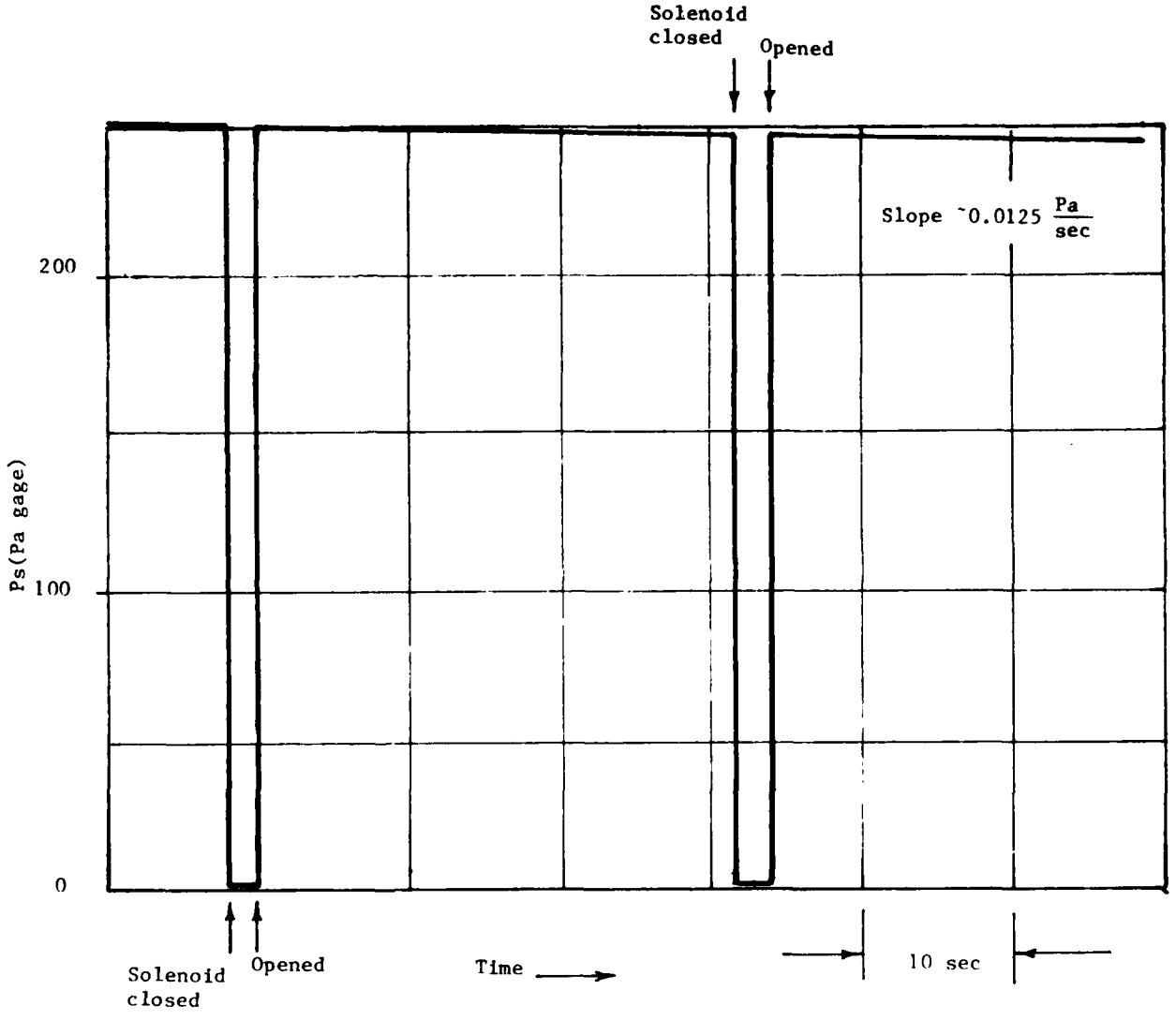

Figure 23. Supply pressure long term drift and response to solenoid valve.

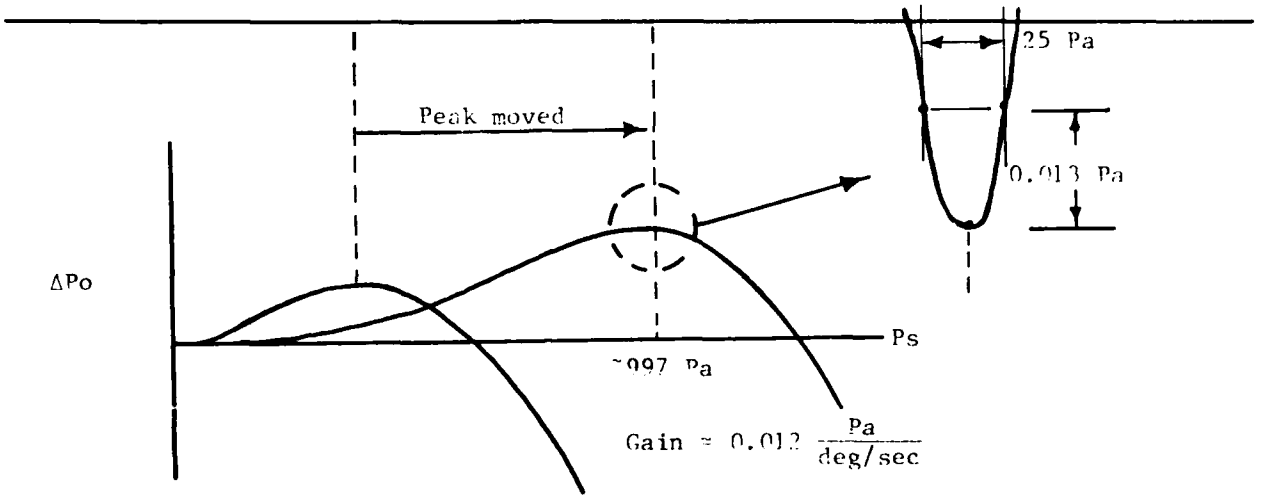

Figure 24. Effect of adjusting nozzle angle.

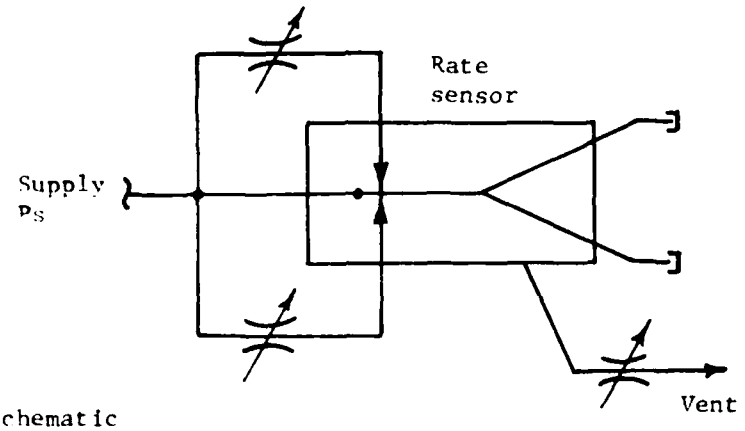

(i) Schematic

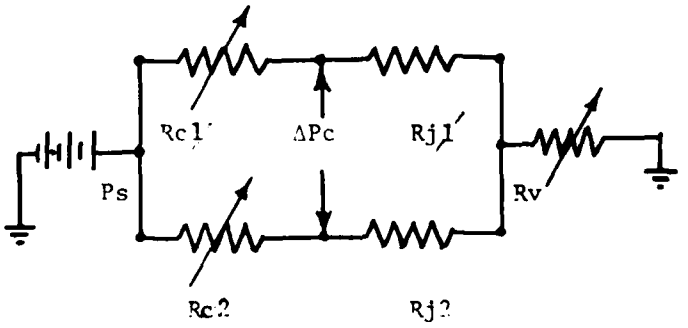

(ii) Equivalent circuit

Figure 25. Biasing technique.

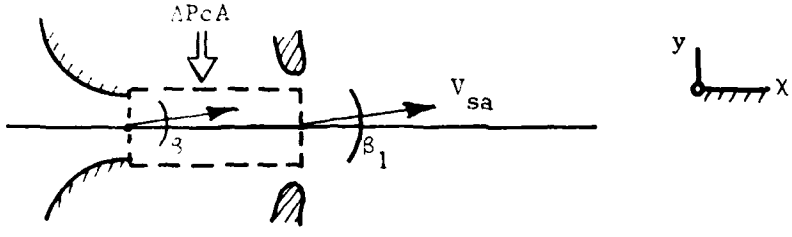

Figure 26. Control volume definition sketch.

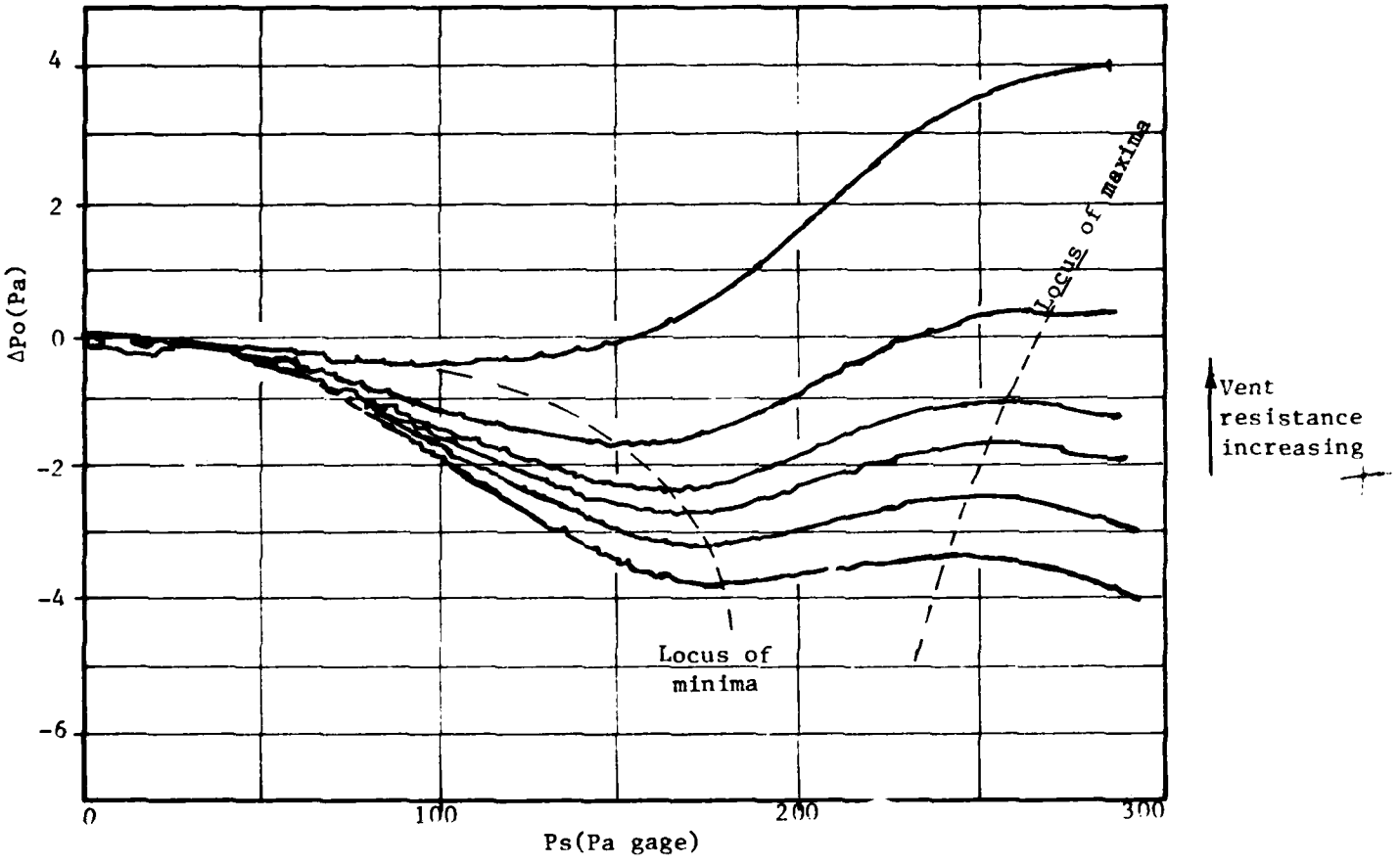

Figure 27. Null behavior, constant bias resistances.

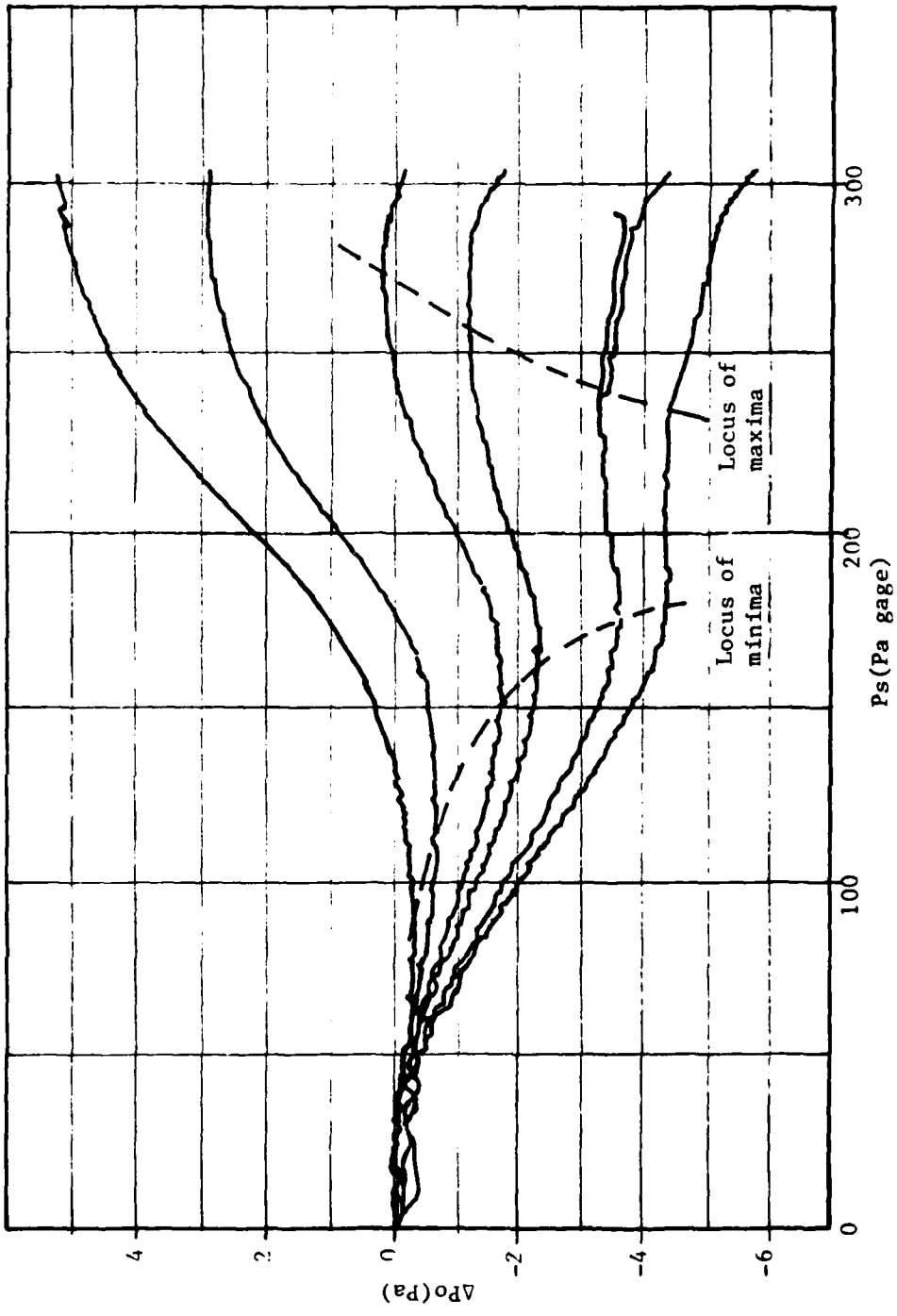

Figure 28. Null behavior, constant vent resistance.

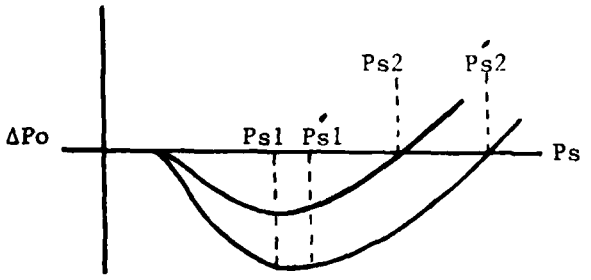

$$\frac{Ps2}{Ps1} = \frac{Ps2'}{Ps1'} = 1.54$$

Figure 29. Relation of zero slope and zero offset points.

NOMENCLATURE

Symbols

B_c	Control port width
B_o	Receiver width
B_s	Nozzle width
B_r	Control edge width
C_D	Nozzle discharge coefficient
C_p	Pressure coefficient
$f( )$	Unspecified function
H	Nozzle height
k, k_1-k_7	Constants (defined in text, as used)
K	Gain
ℓ_{ve}	Equivalent flat plate boundary layer length to produce a proper displacement thickness at nozzle exit
L_R	Distance from nozzle to receiver
$\dot{m}$	Mass flow rate
n	Exponent
N_{Rb}	Reynold's number $V_{sa} B_s/\nu$
Pc	Control port pressure
Po	Output port pressure
Ps	Supply pressure
Q	Volume flow rate
R	Radius
Rc	Resistance of control bias orifice

R_j	Jet control edge resistance
R_v	Vent resistance
t_F	Time of flight of a particle from nozzle to receiver
T	Temperature
V	Velocity
V_p	Potential core velocity
V_{sa}	Average nozzle exit velocity
V_{sp}	Potential core velocity at nozzle exit
W	Width at nozzle entry
X	Boundary layer length
y'	Equivalent flat plate boundary layer length to produce a proper momentum thickness at nozzle exit
x_m	Location of minimum pressure point
x_s	Location of separation point
x_{sp}	Nozzle-to-splitter length
y	Distance perpendicular to wall
$\alpha, \beta, \gamma, \Psi$	Angles (defined in text, as used)
δ	Nominal boundary layer thickness
δ^*	Displacement boundary layer thickness
$\Delta( )$	Difference
ε	Centerline distance along nozzle
Γ	Distance from center of receiver port to center of splitter
μ	Viscosity
ν	Kinematic viscosity, μ/ρ

ω	Angular velocity
Φ	$\equiv (\delta^*)^2$
ρ	Density
σ	Nozzle aspect ratio, H/B_s
τ	Shear stress
Θ	Momentum boundary layer thickness
χ	$\equiv X/B_s$

Subscripts

$( )_E$	Nozzle exit
$( )_t$	Nozzle throat

REFERENCES

1. "Feasibility Investigation of a Laminar Rate Sensor (LARS) Phase I Report", Reader, et al, GE document no. 69SD698, 20 June 1969, Naval Air Systems Command.

2. "Evaluation Program Fluidic Laminar Rate Sensor", Westerman and Wright, MDAC report L0252, 8 March 1974, Naval Air Systesm Command.

3. "A Fluidic Roll Rate Control for High Acceleration Guided Missiles", Onufreiczuk, GE document no. 73SD2041, Interim Report, March 1973, MICOM.

4. "Feasibility Investigation of a LARS, Phase IV Final Report," Young, GE document no. 73SD2147, August 1973, Naval Air Systems Command.

5. "Final Report, Fluidic Roll Rate Control System for High Acceleration Terminal Homing Missiles." Young, GE document no. 745D2053, April 1974, US Army Missile Command.

6. "Feasibility Investigation of a LARS, Phase IV Final Report", Onufreiczuk Young, and Gresham, GE document no. 75SDR2173, April 1975, Naval Air Systems Command.

7. "Fluidic Laminar Angular Rate Sensor Development Program, Final Report", G. W. Roe, MDAC report L0317, 17 April 1975, Naval Air Development Center.

8. "Production of Fluid Amplifiers by Optical Fabrication Techniques", R. W. Van Tillburg, Proceedings of the Fluid Amplification Symposium, October 1962, V-1, p. 143-156.

9. "Some Analytical and Experimental Studies of Laminar Proportional Amplifiers", Shearer and Smith, HDL-CR 76-213-1, April 1976, (Penn State Univ.).

10. Boundary Layer Theory, Schlighting, Mc-Graw Hill, 1968, p. 177.

11. "Approximate Methods for Predicting Separation Properties of Laminar Boundary Layers", Curle and Skan, Aero-Quarterly, Vol. VIII, p. 257, August, 1957.

12. "Analytic Design of Laminar Proportional Amplifiers", Manion and Drzewiecki, Fluidic State-of-the Art Symposium, Vol. I, 30 September - 3 October, 1974, p. 201.

13. "Temperature Effects on Fluidic Laminar Rate Sensor", P. Hsueh, Appendix C of GE document no. 69SD698, 20 June 1969, Air Force Contract no. F33615-68-C-1700.

DISTRIBUTION

	No. of Copies
Defense Technical Information Center Cameron Station Alexandria, Virginia 22314	2
A. R. Barbin M. E. Department Auburn University Auburn, Alabama 36840	2
V. H. Baumgarth ARRADCOM ATTN: DRDAR-SCF-CC Dover, New Jersey 07801	1
John Burmeister Naval Weapons Center ATTN: CODE 3636 China Lake, California 93555	1
James Carr HQ, DOE/GERMANTOWN Mail Stop F309 Washington, DC 20545	1
Peter F. Dixon US Army ARRADCOM ATTN: DRDAR-LCU-M Dover, New Jersey 07801	1
T. M. Drzewiecki HDL, ATTN: DELHD-RT-CD 2800 Powder Mill Road Adelphi, Maryland 20783	1
J. C. Dunaway US Army Missile Command ATTN: DRSMI-RGC, Bldg 5400 Redstone Arsenal, Alabama 35898	1
Keith L. Englander Naval Ordnance Station CODE 5123C Indian Head, Maryland 20640	1
A. J. Garrett Pacific Missile Test Center CODE 3122 Point Mugu, California 93042	1

DISTRIBUTION (Continued)

	No. of Copies
Michael Goes US Army ARRADCOM ATTN: DRDAR-LCN-C Dover, New Jersey 07801	1
John M. Goto HDL, ATTN: DELHD-RT-CD 2800 Powder Mill Road Adelphi, Maryland 20783	1
Richard N. Gottron HDL, ATTN: DELHD-RT-CD 2800 Powder Mill Road Adelphi, Maryland 20783	1
Richard Hellbaum NASA, Langley Center MS 494 Hampton, Virginia 23665	1
Dean Houck Naval Air Systems Command ATTN: AIR 5162C8 Washington, DC 20361	1
Tor Jansen Naval Air Development Center CODE 60134 Warminster, Pennsylvania 18974	1
James W. Joyce Harry Diamond Laboratories ATTN: DELHD-RT-CD 2800 Powder Mill Road Adelphi, Maryland 20783	1
David Keyser Naval Air Development Center CODE 60134 Warminster, Pennsylvania 18974	1
Daniel C. Kinney HQ AFOSI/IVTSR Bolling AFB, DC 20332	1
Keith Klaber Department of Transportation 400 7th Street, SW Washington, DC 20590	

DISTRIBUTION (Continued)

	No. of Copies
T. K. Lau DOE/FE-DART, C-156 Washington, DC 20545	1
R. L. McGiboney Naval Air Development Center CODE 60134 Warminster, Pennsylvania 18974	1
R. Michael Phillippi HDL, ATTN: DELHD-RT-CD 2800 Powder Mill Road Adelphi, Maryland 20783	1
James L. Powell DOE - FE 44 Washington, DC 20545	1
Albertus E. Schmidlin US Army ARRADCOM ATTN: DRDAR-LCN-C, Bldg 65 Dover, New Jersey 07801	1
Gene Spratke US Army TARADCOM ATTN: DRSTA-RCAF Warren, Michigan 48090	1
Bill Waldon Naval Weapons Center China Lake, California 93555	1
James A. Burke HQ, Dept of the Army ATTN: DAMA-WSA Washington, DC 20310	1
John E. Burns Naval Air Systems Command CODE AIR-5162CI Washington, DC 20361	1
George W. Fosdick Applied Technology Laboratory ATTN: DAVOL-ATL-ASA Ft Eustis, Virginia 23604	1
Al Franz US Army ARRADCOM ATTN: DRDAR-LCN-F Dover, New Jersey 07801	1

DISTRIBUTION (Continued)

	No. of Copies
Commander US Army Training and Doctrine Command Ft Monroe, Virginia 23341	1
Commander US Army Combined Arms Combat Development Activity Ft Leavenworth, Kansas 66027	1
Commander US Army Armor Center Directorate for Armor Aviation ATTN: ATSB-AADO-MS, LTC Don Smart FT Knox, Kentucky 40121	1
Headquarters Department of the Army ATTN: DAMA-WSM, MAJ Belch Washington, DC 20310	1
Commander US Naval Weapons Center ATTN: Mr. J. A. Knecht China Lake, California 93555	1
DRCPM-HF	1
-HFE, Mr. J. Service	1
DRSMI-X	1
DRSMI-R, Dr. McCorkle	1
-R, Dr. Rhoades	1
-R, Mr. Black	1
-RG	1
-RGC	20
-RGT	1
-REO	1
-REI	1
-RE	1
-RR, Dr. Hartman	1
-RR, Dr. Guenther	1
-RR, Dr. Gamble	1
-RN, Mr. E. Dobbins	1
-RPR	5
-RPT Reference Copy	1
-RPT Record Copy	1
DRSMI-LP, Mr. Voight	1

Distribution (Concluded)

	No. of Copies
Douglas Garner NASA, Langley Center MS 494 Hampton, Virginia 23665	1
George C. Kopcsak OUSDRE(ET) Pentagon, RM 3E.089 Washington, DC 20301	1
James Papadopoulos SMD Advanced Technology Center P. O. Center 1500 Huntsville, Alabama 35807	1
Ken Reader ASED - CODE 1605 Naval Ship R&D Center Bethesda, Maryland 20084	1
Harry M. Snowball AF Flight Dynamics Laboratory ATTN: AFFDL/FGL Wright-Patterson AFB, Ohio 45433	1
Robert N. Ware US Army MERADCOM ATTN: DRDME-EMA Ft Belvoir, Virginia 22060	

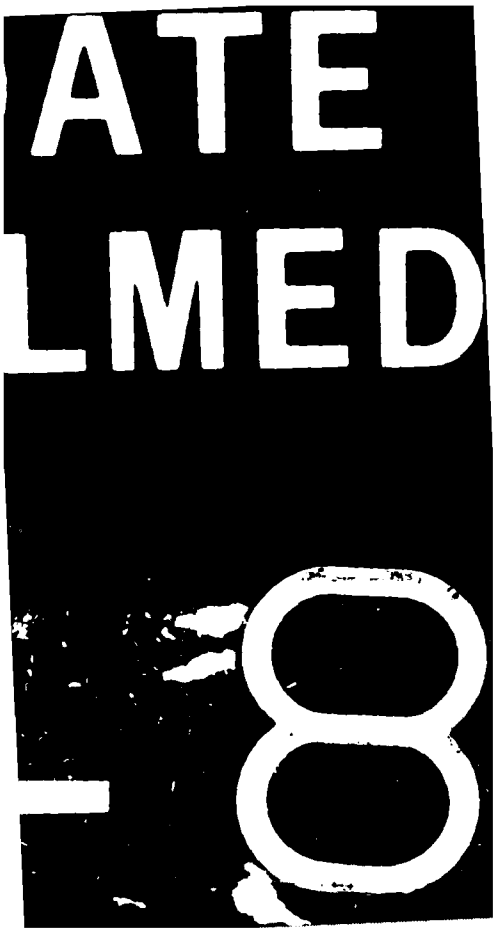
ATE
LMED
8